Environmental Earth Sciences (2023) 82:502
https://doi.org/10.1007/s12665-023-11081-0

ORIGINAL ARTICLE

Two-sided fault parameter assessment through the utilization of a particle swarm optimizer to different gravity horizontal gradients-orders with application to various cases studies

Mahmoud Elhussein[1] · Eid R. Abo-Ezz[2] · Omar A. Gomaa[1] · Yves Géraud[3] · Khalid S. Essa[1]

Received: 24 November 2022 / Accepted: 28 July 2023 / Published online: 30 September 2023

Abstract
Metaheuristic methods are increasingly being implemented to source parameter estimation of gravity anomalies. These approaches have become popular in the geophysical community because of their superior advantages. We emphasize the application of the particle swarm optimizer (PSO), which is motivated by the birds' behaviors, to elucidate gravity anomalies. Besides, using different horizontal derivative orders for the observed data is valuable in reducing the regional field effect. The current inversion algorithm applied to other synthetic models (a two-sided dipping fault with a third-order regional, a two-sided dipping fault model interfered by a spherical structure model with and without 10% noise, and two neighboring two-sided dipping faults models with and without 10% noise) as well as two real-world cases from the United States and Tunisia. The usefulness of applying these techniques together was demonstrated by providing stable results in executing the buried source parameters and eradicating the regional field effect. Therefore, we recommend the application of these techniques in the model parameter estimation studies performed with potential field anomalies due to mineralized zones.

Keywords Modeling · Two-sided fault · Gravity anomalies · Interpretation

Introduction

Gravity exploration method has traditionally been utilized to assess and describe the variant in subsurface rock densities and offer an important understanding sight of the subsurface geology (Nabighian et al. 2005; Abdelrahman et al. 2013; Rezaie 2019; Kumar et al. 2020; Gadirov et al. 2022; Essa and Diab 2023). The assessment of model parameters of buried source bodies is a vital step in gravity anomaly elucidation (Abdelrahman and Essa 2015; Essa and Géraud 2020; Ekinci et al. 2021). It is utilized to predict the geothermal potential reservoir parameters (i.e., location, depth) and also used in several geophysical investigations such as hydrocarbon exploration, cavities and tunnels detection, ore and mineral exploration, archeological sites investigation, and geological features or formations that exist beneath the surface of the Earth (Ekinci and Yiğitbaş, 2015; Essa et al. 2020, 2022; Dilalos and Alexopoulos 2020; Rosid and Saraswati 2020; Young et al. 2020; Guglielmetti and Moscariello 2021; Kheyrollahi et al. 2021; Chavanidis et al. 2022; Saleh et al. 2022; Wang et al. 2022).

There are several methods established to infer gravity data, i.e., Asfahani and Tlas (2012) presented an approach that combined Fair function minimisation and stochastic optimisation to inferring residual gravity anomalies for spherical and cylindrical model structures. Chakravarthi et al. (2016) developed two algorithms in the space-domain to scrutinize gravity anomalies for sedimentary basins by an exponential-density function. Tlas and Asfahani (2018) mentioned an easy interpretation method for gravity anomalies depending on the quadratic curve regression. Essa et al. (2020) described a fast imaging technique called "the R-parameter imaging technique" for inferring gravity data acquired along profiles. Essa et al. (2021c) developed an inversion algorithm based on the utilization of the analytic

✉ Khalid S. Essa
khalid_sa_essa@cu.edu.eg; essa@cu.edu.eg

[1] Department of Geophysics, Faculty of Science, Cairo University, P.O. 12613, Giza, Egypt

[2] Department of Physics, College of Science and Humanities, Prince Sattam Bin Abdulaziz University, 11942 Al-Kharj, Saudi Arabia

[3] GeoRessources Laboratory, University of Lorraine, 54500 Nancy, France

signal to investigate gravity profiles. Mehanee (2022) developed a nonlinear optimization algorithm for inverting the gravity profile for a 2D faulted thin block and was dependent on the simultaneous algorithm optimization.

Moreover, the utilization of metaheuristic optimization algorithms (particle swarm, simulated annealing, genetic, differential evolution, ant colony, cuckoo search, bat, …, etc.) has been used too much in the geophysical data inversion and given stable results. For example, Datta et al. (2012) used an ant colony algorithm to elucidate a total gradient potential field. Toushmalani and Saibi (2015) applied a cuckoo search for inverting 3D gravity data. Ekinci et al. (2016) proposed a useful use for differential evolution (DE) to interpret residual gravity anomalies. Essa and Munschy (2019) described a method that depends on using a particle swarm optimizer (PSO) for inferring second-moving average gravity anomalies. Rao and Biswas (2021) used simulated annealing to infer gravity anomalies due to 2-D faults. Essa and Diab (2023) used the Bat algorithm to infer 2-D gravity anomaly profiles for geothermal exploration and volcanic activity.

Using a deductive awareness of either density or geometry, it is possible to identify fault structures and reduce the complexity of parameter space for gravity inversion. This approach enables a distinctive solution to be obtained, which can help in understanding the subsurface geology and potential mineral resources. For instance, if the density of the fault zone is known from geological observations, this information can be used as a constraint for gravity inversion, which can then provide a better estimate of the position and geometry of the fault. Similarly, if the geometry of the fault is well-defined from seismic or other geophysical data, this information can be used as a constraint for gravity inversion, which can then provide a more precise guess of the density distribution within the fault zone. Overall, using a deductive approach to assessing fault structure can improve the reliability and accuracy of gravity inversion techniques, and ultimately help in making more informed decisions for resource exploration and management. The process of utilizing gravity data inversion to assess basement relief continues to be employed, despite limited information about basement depth from a small number of boreholes and no prior knowledge of density contrast. When it comes to solving these problems, global optimization algorithms have a significant edge over local optimization algorithms. Global optimization techniques can address complex criteria without requiring an initial model to be preset.

Structure assessment of dipping faults is also of significant concern in applied geophysics for adequately understanding the advancement of various geological features. Faults belong to the most valuable geological structures for regional studies and specific other explorations. Recognizing regional faulting and tectonic risks involves knowing the subsurface the structure and behavior of dipping faults, which is crucial for both scientific investigations and practical applications in the energy and mining industries. Therefore, many researchers designed optimization techniques for accurately predicting fault geometric features using global and local optimization algorithms (Roy and Kumar 2021; Nibisha et al. 2022; Roy et al. 2022).

In this paper, we explained how to infer 2D gravity anomalies for faults along profiles by determining their characteristic parameters through the usage of a particle swarm optimizer method (PSO) for the various-order of the gravity horizontal gradient. The benefit of using these gradients is fallen on eliminating the regional field effect. The efficacy of the current inversion algorithm was confirmed by different synthetic models with different scenarios. Practically, it is corroborated by two field data sets from USA and Tunisia. The results from this scheme were compared with available results from drilling, geology, and other used methods.

Methods

Forward modeling

Gravity anomaly along the profile in the Cartesian coordinate system for any geometric style represented by two-sided dipping faults (Fig. 1) is (Essa 2013; Essa et al. 2021a):

$$g\left(x_i, x_o, z_{\text{up}}, z_{\text{down}}, M, \theta\right) = M\left[1 + \frac{1}{\pi}\tan^{-1}\left(\frac{\left(x_i - x_o\right)}{z_{\text{up}}} + \cot\theta\right) - \frac{1}{\pi}\tan^{-1}\left(\frac{\left(x_i - x_o\right)}{z_{\text{down}}}\right) + \cot\theta\right], \tag{1}$$

where x_i and x_o (m) signify the locations of the collected measurement points and fault trace origin, $M = 2\pi f \Delta\sigma t \times 10^5$ (mGal) and called the amplitude coefficient, t is the thickness (m) of the layer, $f = 6.67 \times 10^{-11}\left(\frac{\text{m}^3}{\text{kg}\times\text{s}^2}\right)$, z_{up} and z_{down}

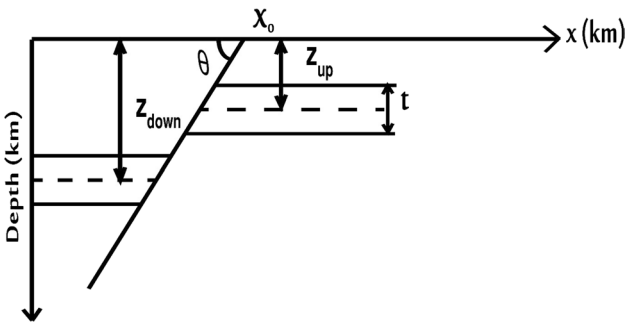

Fig. 1 Schematic illustration shows a two-sided dipping fault source with its parameters

represent depths to upthrown downthrown parts, and θ is the dip angle of faults.

Formulation of the inverse scheme

Using different orders of horizontal derivatives was considered a pioneering technique to diminish the effect of the regional gravity anomaly. For example, Essa and Munschy (2019) mentioned the first-order group. Here, we described along the profiles the third horizontal derivative anomaly (Δg_{xxx}), which is given as

$$\Delta g_{xxx}(x_i, s) = \frac{g(x_i + 3s) - 3g(x_i) + 3g(x_i) - g(x_i - 3s)}{8s^3} \tag{2}$$

and the fourth horizontal derivative anomaly (Δg_{xxxx}) is

$$\Delta g_{xxxx}(x_i, s) = \frac{g(x_i + 4s) - 4g(x_i + 2s) + 6g(x_i) - 4g(x_i - 2s) + g(x_i - 4s)}{16s^4} \tag{3}$$

where s represents the window length.

The particle swarm optimizer (PSO)

To deal with extremely nonlinear issues, recent trends employ evolutionary, stochastic heuristic and nature-inspired algorithms. Differential evolution, particle swarm optimizer, cuckoo search, and firefly algorithms are examples of nature-inspired algorithms that are simple and efficient at explaining a wide range of real-world issues.

In this paper, the applied algorithm is the particle swarm optimizer (PSO) was recognized by Eberhart and Kennedy (1995) and inspired by the bird's search for food in nature. The birds presented particles that work in the search field to find the solution. More applications for this algorithm are found in Singh and Biswas (2016), Anderson et al. (2020), and Essa et al. (2022).

The process was initiated by randomly distributing particles for the swarm and then proceeds to search for sources through successive generations. At each step, the velocities and locations of the particles are adjusted using the following formulas:

$$v_j^{L+1} = c_3 v_j^L + c_1 \text{ rand}\left(T_{\text{best}} - x_j^{L+1}\right) + c_2 \text{ rand}\left(J_{\text{best}} - x_j^{L+1}\right), \tag{4}$$

$$x_j^{L+1} = x_j^L + v_j^{L+1}, \tag{5}$$

where x_j^L is the present location of the jth particle at the L$^{\text{th}}$ iteration, v_j^L signifies the velocity of the jth particle at the Lth iteration, random numbers amongst [0,1] has been used using the rand function, (c_1, c_2, and c_3) are some controlling factors of the convergence. The parameter c_1 serves as a cognitive parameter that facilitates the individual exploration of the particles, c_2 is a social parameter that guides the particles to a global direction, and the inertial factor, c_3, adjusts the speed of particles. T_{best} is the best location, which is acquired by a model, while J_{best} is the best global place reached by any particle in the swarm. Afterwards, the achieved best solution (T_{best}) and the global best solution (J_{best}) are stored in memory. The model's velocity and place are updated through an iteration procedure, which terminates when the convergence.

Here, finding the global minimum for this scheme is done by applying a suitable objective function. Therefore, the following objective functional ($\mathcal{K}_{\text{objective}}$) is utilized to execute the dipping fault using the gravity data (M, z_{up}, z_{down}, x_{o}, and Θ):

$$\mathcal{K}_{objective} = \sqrt{\frac{1}{u}\sum_{i=1}^{u}\left[\Delta g_j^{obs}(x_j) - \Delta g_j^{calc}(x_j)\right]^2} \tag{6}$$

where u signify the number of data points, Δg_j^{obs} represents the observed gravity field data and Δg_j^{calc} represents the calculated gravity field data.

The flowchart of the procedures for estimating the model parameters is represented in Fig. 2 and in the incoming steps:

The gravity data of the profile is read as the first step of the procedure, then applying the different horizontal derivatives in the second step (Third, Fourth) to reduce the effect of the regional data with different orders (Eqs. 2, 3). Applying the code of the (PSO) particle swarm optimization will come as a third step to appraise the dipping fault parameters, which consider the best parameters of the fault, while the particles reach the global minimum by updating their velocity and location for each parameter. Finally, the forward model (Eq. 1) is developed using the derived parameters to investigate the discrepancy amongst the calculated and observed gravity anomalies.

The parameters of the tuning PSO scheme were selected according to various studies of several parameter groups (Fig. 3 and Table 1) and the suitable parameters are $c_1 = c_2 = 2$ and $c_3 = 0.9$ (rapid convergence rate).

Synthetic models studies

To confirm the application of the proposed PSO approach in gravity data, several simulated data sets were examined to determine the subsurface model parameters as follows:

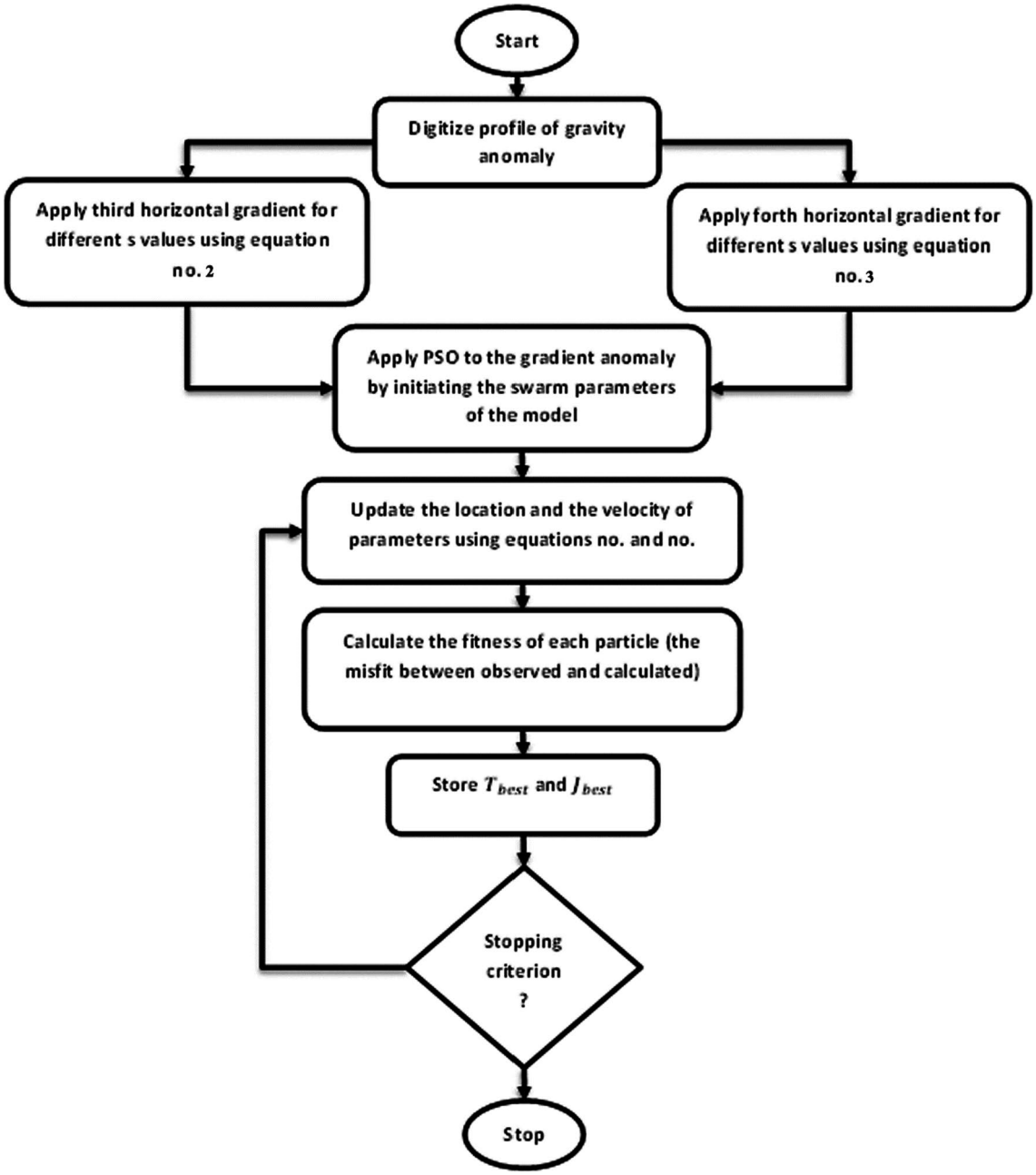

Fig. 2 PSO scheme inversion process flowchart

Model 1: effect of a regional field

The observed gravity profile (140 km) was created and consisted of a two-sided fault example ($M = 390$ mGal, $z_{up} = 6$ km, $\theta = 40°$, $z_{down} = 9$ km, and $x_0 = 70$ km) with a third-order regional field background. It was examined in two manners as follows:

First, the third horizontal gradient was employed for this anomaly utilizing numerous s values ($s = 2$, 3, 4, 5, 6, 7, 8, 9, and 10 km) (Fig. 4a). The PSO scheme was used to evaluate the fault parameters (Table 2). The predicted parameters are $M = 383.2 \pm 5.67$ mGal, $z_{up} = 6.77 \pm 0.19$ km, $\theta = 45.98 \pm 0.94°$, $z_{down} = 8.47 \pm 0.16$ km, $x_o = 72.12 \pm 0.75$ km, and the root mean square of the error (RMS error) = 11.0187 mGal.

Second, Fig. 4b displays the observed and expected parameters of the two-sided fault by applying the PSO to the fourth horizontal derivatives anomalies (Table 3)

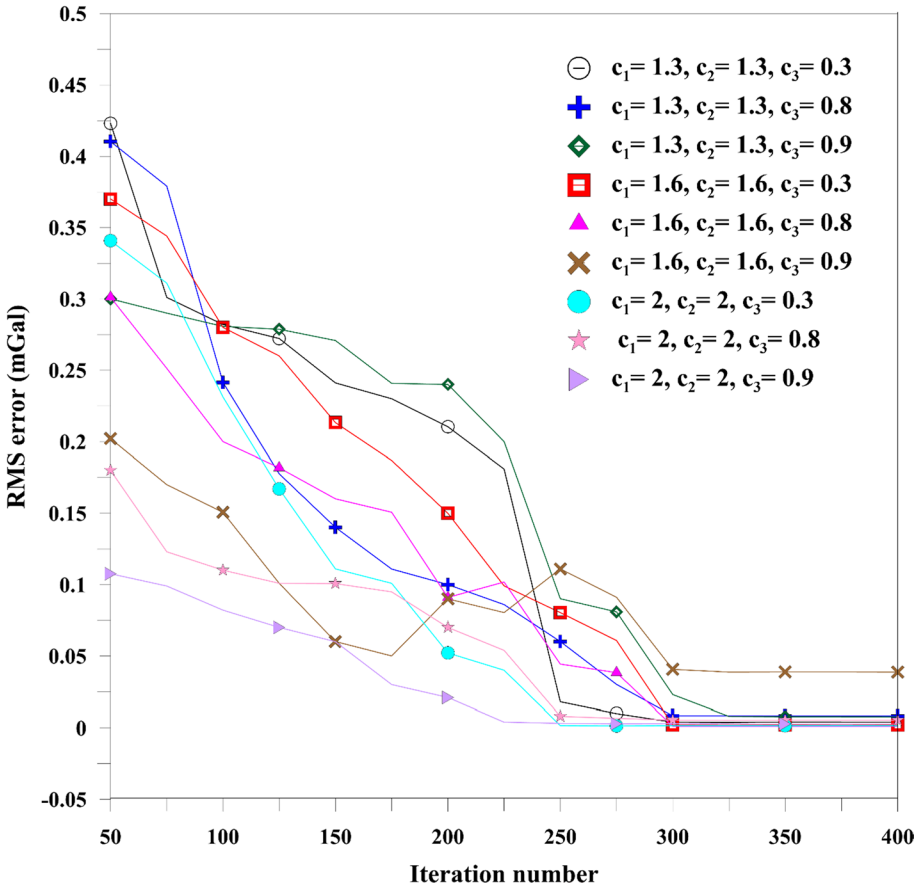

Fig. 3 PSO-controls parameters (c_1, c_2, and c_3) effect on rate of convergence

Table 1 Model 1: Influence of the parameters c_1, c_2 and c_3 on the convergence rate (Fig. 3)

Parameters	RMS error (mGal)								
	$c_1, c_2=1.3$ $c_3=0.3$	$c_1, c_2=1.3$ $c_3=0.8$	$c_1, c_2=1.3$ $c_3=0.9$	$c_1, c_2=1.6$ $c_3=0.3$	$c_1, c_2=1.6$ $c_3=0.8$	$c_1, c_2=1.6$ $c_3=0.9$	$c_1, c_2=2$ $c_3=0.3$	$c_1, c_2=2$ $c_3=0.8$	$c_1, c_2=2$ $c_3=0.9$
Iterations									
50	0.4231	0.4103	0.3001	0.3701	0.3012	0.2022	0.3408	0.1801	0.1077
75	0.3011	0.3791	0.2901	0.3441	0.2514	0.1701	0.3111	0.1231	0.0991
100	0.2821	0.2415	0.2808	0.2801	0.2001	0.1507	0.2313	0.1102	0.0822
125	0.2723	0.1777	0.2788	0.2601	0.1819	0.101	0.1671	0.101	0.0701
150	0.2412	0.1402	0.2709	0.2134	0.1602	0.0602	0.1111	0.1008	0.0601
175	0.2301	0.111	0.2409	0.187	0.1508	0.0501	0.101	0.095	0.0301
200	0.2105	0.1001	0.2401	0.1501	0.0911	0.0901	0.0522	0.0701	0.0211
225	0.181	0.0861	0.2001	0.0992	0.1019	0.0805	0.0401	0.054	0.0041
250	0.0181	0.0602	0.0902	0.0805	0.0444	0.1111	0.0017	0.0081	0.0033
275	0.01	0.0302	0.081	0.0609	0.0384	0.0912	0.0015	0.0068	0.003
300	0.0041	0.0085	0.0231	0.0021	0.0013	0.0407	0.0017	0.0055	0.0031
325	0.0039	0.0085	0.0081	0.002	0.0013	0.0388	0.0017	0.0054	0.0029
350	0.0042	0.0084	0.0079	0.0021	0.0013	0.0389	0.0017	0.0055	0.0028
375	0.0042	0.0084	0.0079	0.002	0.0013	0.0389	0.0017	0.0055	0.0028
400	0.0041	0.0084	0.0078	0.0021	0.0013	0.0388	0.0017	0.0055	0.0028

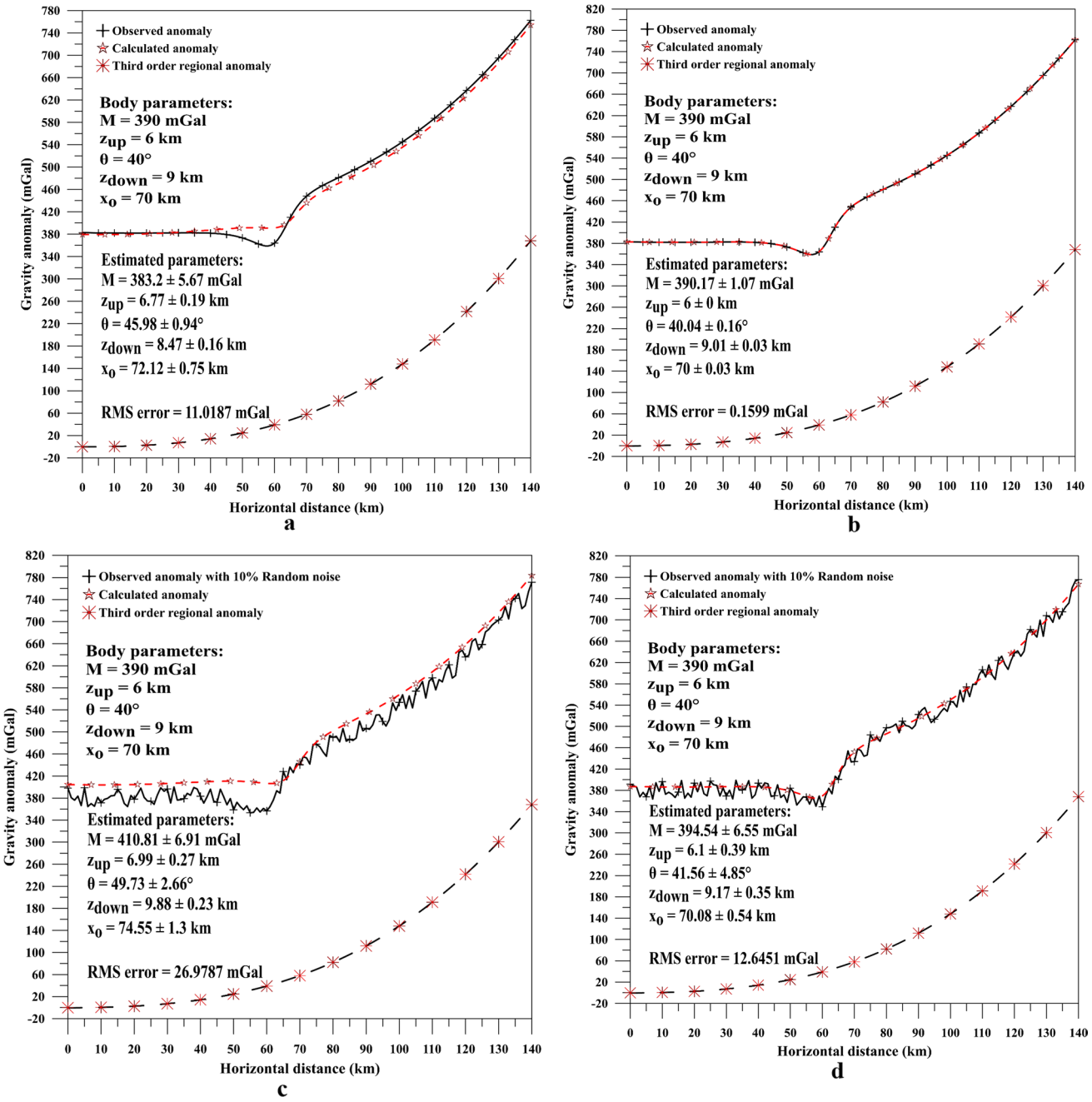

Fig. 4 **a** Gravity anomaly represents Model 1 in case using a third horizontal gradient method. **b** Gravity anomaly represents Model 1 in case using a fourth horizontal gradient method. **c** Gravity anomaly represents Model 1 with a 10% noise in case using a third horizontal gradient method. **d** Gravity anomaly represents Model 1 with a 10% noise in case using a fourth horizontal gradient method

and the predicted parameters are $M = 390.17 \pm 1.07$ mGal, $z_{up} = 6 \pm 0$ km, $\theta = 40.04 \pm 0.16°$, $z_{down} = 9.01 \pm 0.03$ km, $x_o = 70 \pm 0.03$ km, and RMS error = 0.1599 mGal.

Third, Fig. 4c displays the observed and expected parameters of the two-sided fault via using the PSO to the third horizontal derivatives anomalies in case of 10% random noises (Table 2) and the predicted parameters are $M = 410.81 \pm 6.91$ mGal, $z_{up} = 6.99 \pm 0.27$ km, $\theta = 49.73 \pm 2.66°$, $z_{down} = 9.88 \pm 0.23$ km, $x_o = 74.55 \pm 1.3$ km, and RMS error = 26.9787 mGal.

Fourth, Fig. 4d displays the observed and expected parameters of the two-sided fault through utilizing the PSO to the fourth horizontal derivatives anomalies with 10% random noises (Table 3) and the predicted

Table 2 Model 1: Results of the PSO-inversion algorithm applied to third horizontal derivative anomalies of the gravity profile (140 km) due to composite anomaly of two-sided dipping fault model (M = 390 mGal, z_{up} = 6 km, θ = 40°, z_{down} = 9 km and x_0 = 70 km) and third-order regional

Parameters	Used ranges	Results											
		Noise-free case											
		s = 2 km	s = 3 km	s = 4 km	s = 5 km	s = 6 km	s = 7 km	s = 8 km	s = 9 km	s = 10 km	ϕ	Error (%)	RMS error (mGal)
M (mGal)	200–800	377.41	397	381.67	379.71	382.03	384	385.3	381.7	380	383.2 ± 5.67	1.74	11.02
z_{up} (km)	2–9	6.9	6.7	6.5	6.8	7.1	6.7	6.5	6.8	6.9	6.77 ± 0.19	12.78	
θ (degree)	20–120	45.6	44.74	45.05	46.04	47.1	47.43	46.57	46.15	45.13	45.98 ± 0.94	14.95	
z_{down} (km)	5–14	8.4	8.6	8.5	8.6	8.2	8.3	8.4	8.7	8.5	8.47 ± 0.16	5.93	
x_o (km)	60–80	73	72.05	71.89	72.41	73.09	71.55	71.3	72.79	71	72.12 ± 0.75	3.03	
10% random noise case													
M (mGal)	200–800	415.09	419.6	409.08	411.08	415.3	400	402.74	406.01	418.4	410.81 ± 6.91	5.3362	26.97
z_{up} (km)	2–9	6.9	7.4	7.2	6.8	6.7	7.3	6.7	6.8	7.1	6.99 ± 0.27	16.4815	
θ (degree)	20–120	52.03	55.04	49.23	48.01	50.04	47.2	48.25	46.69	51.06	49.73 ± 2.66	24.3194	
z_{down} (km)	5–14	9.9	9.8	9.9	10.3	9.7	9.8	10.1	9.9	9.5	9.88 ± 0.23	9.7531	
x_o (km)	60–80	74	74.99	73.76	73.48	72.82	74.08	76	76.98	74.81	74.55 ± 1.3	6.4952	

Table 3 Model 1: Results of the PSO-inversion algorithm applied to fourth horizontal derivative anomalies of the gravity profile (140 km) due to composite anomaly of two-sided dipping fault model (M = 390 mGal, z_{up} = 6 km, θ = 40°, z_{down} = 9 km and x_0 = 70 km) and third-order regional

Parameters	Used ranges	Results											
		Noise-free case											
		s = 2 km	s = 3 km	s = 4 km	s = 5 km	s = 6 km	s = 7 km	s = 8 km	s = 9 km	s = 10 km	ϕ	Error (%)	RMS error (mGal)
M (mGal)	200–800	389.23	392	391.02	389.6	390.2	390	391.04	390	388.43	390.17 ± 1.07	0.04	0.16
z_{up} (km)	2–9	6	6	6	6	6	6	6	6	6	6 ± 0	0.00	
θ (degree)	20–120	40.21	39.71	40.29	39.99	40.06	40	40.05	40	40.01	40.04 ± 0.16	0.09	
z_{down} (km)	5–14	9	9	9	9	9	9.1	9	9	9	9.01 ± 0.03	0.12	
x_o (km)	60–80	69.96	70.06	69.95	70	70	70	70	70	70	70 ± 0.03	0.00	
10% random noise case													
M (mGal)	200–800	387.96	395.67	405.51	386.5	394.6	398.24	386.13	399.55	396.69	394.54 ± 6.55	1.1638	12.64
z_{up} (km)	2–9	5.6	5.7	6.4	6.5	5.8	6.3	5.7	6.5	6.4	6.1 ± 0.39	1.6667	
θ (degree)	20–120	43.12	37.77	43.05	45.96	37.9	46.16	36.57	48.46	35.01	41.56 ± 4.85	3.8889	
z_{down} (km)	5–14	8.7	9.3	8.6	9.4	9.5	9.2	8.9	9.4	9.5	9.17 ± 0.35	1.8519	
x_o (km)	60–80	69.72	70.86	70.57	70.18	69.74	70.73	69.56	70.04	69.33	70.08 ± 0.54	0.1159	

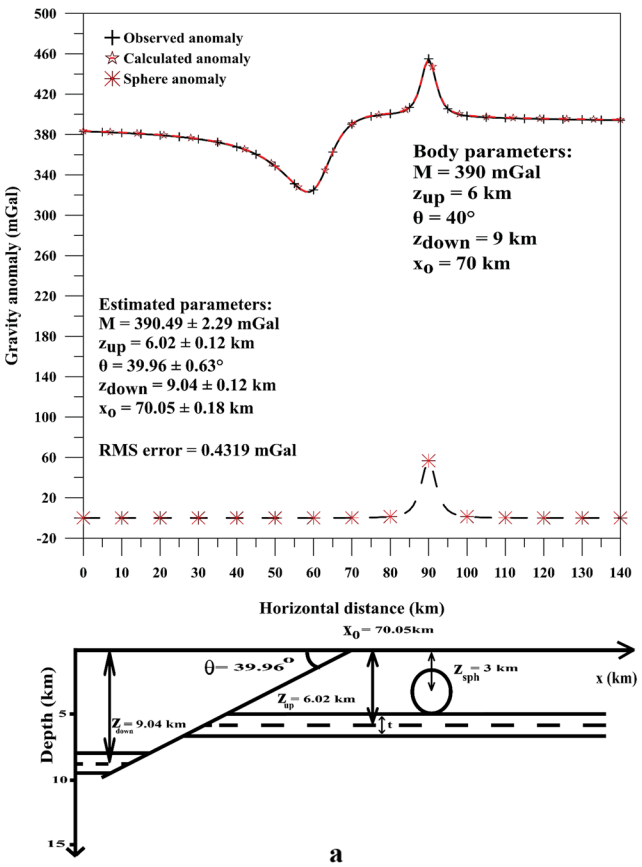
Observed anomaly
Calculated anomaly
Sphere anomaly
Body parameters:
M = 390 mGal
zup = 6 km
θ = 40°
zdown = 9 km
xo = 70 km
Estimated parameters:
M = 390.49 ± 2.29 mGal
zup = 6.02 ± 0.12 km
θ = 39.96 ± 0.63°
zdown = 9.04 ± 0.12 km
xo = 70.05 ± 0.18 km
RMS error = 0.4319 mGal
Gravity anomaly (mGal)
Horizontal distance (km)
xo= 70.05km
θ= 39.96°
Zup= 6.02 km
Zsph= 3 km
Zdown= 9.04 km
t
x (km)
Depth (km)
a

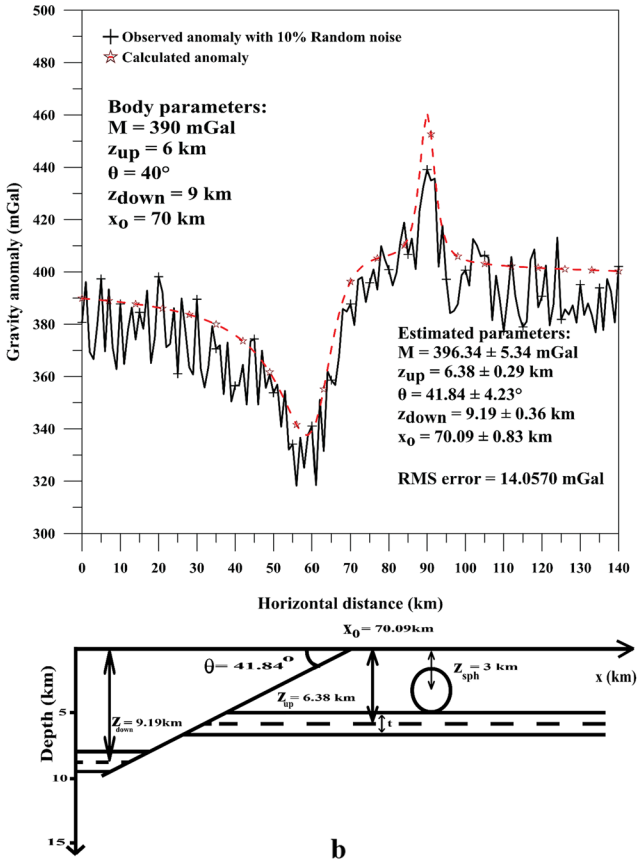
Observed anomaly with 10% Random noise
Calculated anomaly
Body parameters:
M = 390 mGal
zup = 6 km
θ = 40°
zdown = 9 km
xo = 70 km
Estimated parameters:
M = 396.34 ± 5.34 mGal
zup = 6.38 ± 0.29 km
θ = 41.84 ± 4.23°
zdown = 9.19 ± 0.36 km
xo = 70.09 ± 0.83 km
RMS error = 14.0570 mGal
Gravity anomaly (mGal)
Horizontal distance (km)
xo= 70.09km
θ= 41.84°
Zup= 6.38 km
Zsph= 3 km
Zdown= 9.19km
t
x (km)
Depth (km)
b

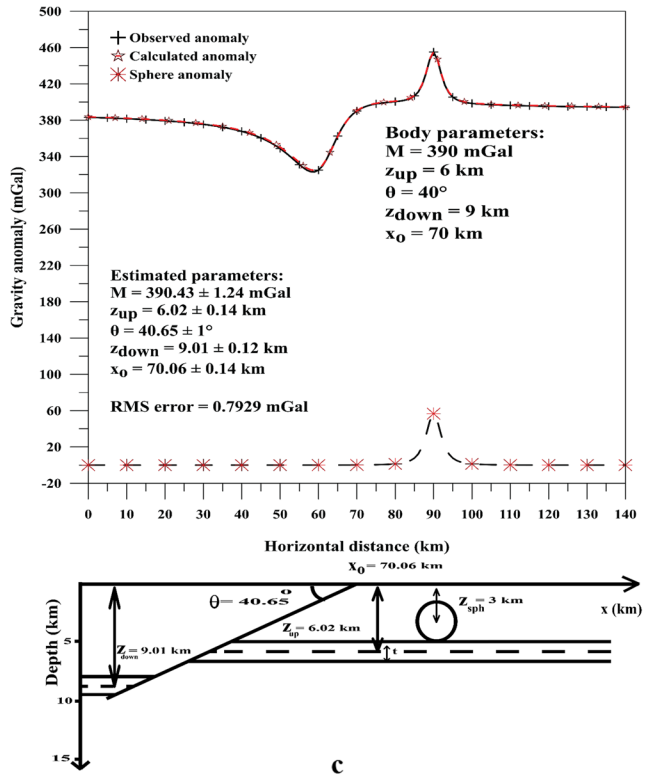
Observed anomaly
Calculated anomaly
Sphere anomaly
Body parameters:
M = 390 mGal
zup = 6 km
θ = 40°
zdown = 9 km
xo = 70 km
Estimated parameters:
M = 390.43 ± 1.24 mGal
zup = 6.02 ± 0.14 km
θ = 40.65 ± 1°
zdown = 9.01 ± 0.12 km
xo = 70.06 ± 0.14 km
RMS error = 0.7929 mGal
Gravity anomaly (mGal)
Horizontal distance (km)
xo= 70.06 km
θ= 40.65°
Zup= 6.02 km
Zsph= 3 km
Zdown= 9.01 km
t
x (km)
Depth (km)
c

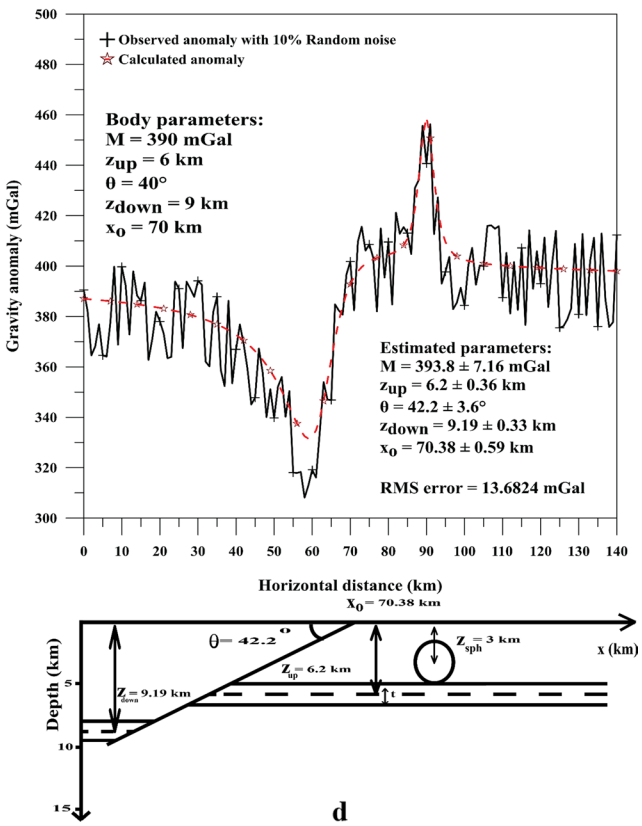
Observed anomaly with 10% Random noise
Calculated anomaly
Body parameters:
M = 390 mGal
zup = 6 km
θ = 40°
zdown = 9 km
xo = 70 km
Estimated parameters:
M = 393.8 ± 7.16 mGal
zup = 6.2 ± 0.36 km
θ = 42.2 ± 3.6°
zdown = 9.19 ± 0.33 km
xo = 70.38 ± 0.59 km
RMS error = 13.6824 mGal
Gravity anomaly (mGal)
Horizontal distance (km)
xo= 70.38 km
θ= 42.2°
Zup= 6.2 km
Zsph= 3 km
Zdown= 9.19 km
t
x (km)
Depth (km)
d

◂**Fig. 5** **a** Gravity anomaly represents Model 2 without noise in case using a third horizontal gradient method. **b** Gravity anomaly represents Model 2 with a 10% noise in case using a third horizontal gradient method. **c** Gravity anomaly represents Model 2 without noise in case using a fourth horizontal gradient method. **d** Gravity anomaly represents Model 2 with a 10% noise in case using a fourth horizontal gradient method

parameters are $M = 394.54 \pm 6.55$ mGal, $z_{up} = 6.1 \pm 0.39$ km, $\theta = 41.56 \pm 4.85°$, $z_{down} = 9.17 \pm 0.35$ km, $x_o = 70.08 \pm 0.54$ km, and RMS error = 12.6451 mGal.

The obtained results demonstrate that the suggested method can produce accurate fault parameters and is capable of minimizing the influence of regional background and noise.

Model 2: effect of interference structures

To study the influence of structures interference, a gravity profile of 140 km was produced for combined two-sided fault and spherical structures with $M = 390$ mGal, $z_{up} = 6$ km, $\theta = 40°$, $z_{down} = 9$ km and $x_0 = 70$ km (fault) and $z_{sphere} = 3$ km, $M_{sphere} = 510$ mGal, $x_{o\ sphere} = 90$ km (sphere) without and with 10% random noise. The interpretation procedures are done as the following consequence:

First, the third horizontal gradient was employed for this anomaly, applying s values equal to 2, 3, 4, 5, 6, 7, 8, 9, and 10 km (Fig. 5a). Then, the PSO scheme was engaged to guess the fault parameters (Table 4) and are $M = 390.49 \pm 2.29$ mGal, $z_{up} = 6.02 \pm 0.12$ km, $\theta = 39.96 \pm 0.63°$, $z_{down} = 9.04 \pm 0.12$ km, $x_o = 70.05 \pm 0.18$ km and RMS error equals 0.439 mGal for a noise-free anomaly. In case of including a 10% noise, Fig. 5b shows the observed and the expected anomalies, and the parameters are $M = 396.34 \pm 5.34$ mGal, $z_{up} = 6.38 \pm 0.29$ km, $\theta = 41.84 \pm 4.23°$, $z_{down} = 9.19 \pm 0.36$ km, $x_o = 70.09 \pm 0.83$ km, and RMS error = 14.0570 mGal (Table 4).

Second, the fourth horizontal gradient was used for the same anomaly with the equivalent s values (Fig. 5c), and the deduced fault parameters are $M = 390.43 \pm 1.24$ mGal, $z_{up} = 6.02 \pm 0.14$ km, $\theta = 40.65 \pm 1°$, $z_{down} = 9.01 \pm 0.12$ km, $x_o = 70.06 \pm 0.14$ km, and RMS error = 0.79 mGal (in a case of noise-free) (Table 5). In addition, in case of including a 10% noise, Fig. 5d shows the observed and the derived anomalies, and the deduced parameters are $M = 393.8 \pm 7.16$ mGal, $z_{up} = 6.2 \pm 0.36$ km, $\theta = 42.2 \pm 3.6°$, $z_{down} = 9.19 \pm 0.33$ km, $x_o = 70.38 \pm 0.59$ km, and RMS equals 13.6824 mGal.

Model 3: effect of multi-faults (horst model)

A 140-km gravity anomaly was created through two neighboring two-sided faults consisting of a horst model with $M_1 = 410$ mGal, $z_{sh} = 3$ km, $\theta_1 = 55°$, $z_1 = 7$ km, $x_{o1} = 50$ km and $M_2 = 460$ mGal, $z_{sh} = 3$ km, $\theta_2 = 30°$, $z_2 = 5$ km, $x_{o2} = 80$ km (Fig. 6a). The interpretation procedures as declared above are:

First (using the third horizontal gradient method), Fig. 6a displays the observed and predicted anomalies of the two neighboring faults with $M_1 = 410.21 \pm 1.4$ mGal, $z_{sh} = 2.99 \pm 0.06$ km, $\theta_1 = 55 \pm 0.15°$, $z_1 = 7.06 \pm 0.05$ km, $x_{o1} = 49.99 \pm 0.01$ km, $M_2 = 462.45 \pm 1.91$ mGal, $z_2 = 4.99 \pm 0.06$ km, $\theta_2 = 29.98 \pm 0.09°$, $x_{o2} = 80 \pm 0.01$ km (in case of noise-free) and RMS error is 2.6953 mGal. Moreover, in the case of a 10% noise included, Fig. 6b shows the observed and predicted anomalies with an RMS error of 27.36 mGal, and the deduced parameters are $M_1 = 414.55 \pm 6.58$ mGal, $z_{sh} = 3.11 \pm 0.47$ km, $\theta_1 = 55.86 \pm 3.34°$, $z_1 = 7.06 \pm 0.53$ km, $x_{o1} = 49.67 \pm 0.81$ km, $M_2 = 464.94 \pm 6.24$ mGal, $z_2 = 5.14 \pm 0.4$ km, $\theta_2 = 31.93 \pm 3.59°$, $x_{o2} = 79.94 \pm 0.67$ km (Table 6).

Second (using the fourth horizontal gradient method), Fig. 6c shows the observed and predicted anomalies and their deduced parameters ($M_1 = 410.81 \pm 1.11$ mGal, $z_{sh} = 2.99 \pm 0.06$ km, $\theta_1 = 54.98 \pm 0.16°$, $z_1 = 7.03 \pm 0.07$ km, $x_{o1} = 50 \pm 0.01$ km, $M_2 = 461.23 \pm 1.15$ mGal, $z_2 = 4.99 \pm 0.08$ km, $\theta_2 = 30.03 \pm 0.19°$, $x_{o2} = 80 \pm 0.04$ km) and RMS error is 2.0266 mGal (Table 7). In addition, after adding a 10% random noise, Fig. 6d displays the observed and predicted anomalies with $M_1 = 412.49 \pm 3.9$ mGal, $z_{sh} = 3.08 \pm 0.41$ km, $\theta_1 = 54.2 \pm 3.92°$, $z_1 = 6.93 \pm 0.41$ km, $x_{o1} = 50.24 \pm 0.84$ km, $M_2 = 462.42 \pm 6.72$ mGal, $z_2 = 4.87 \pm 0.43$ km, $\theta_2 = 31.44 \pm 3.78°$, $x_{o2} = 79.28 \pm 0.25$ km) and RMS error equals 24.3930 mGal.

The combination of input model parameters and outputs are the tactical factors. Sensitivity evaluation is an approach for evaluating the reliability of a model or a judgment. Numerous methods can be used to envision the global model and diminish outcome uncertainty (Feng 2021; Essa et al. 2022). In deciding on the finest control systems, the significance of each control factor ($c1$, $c2$, and $c3$) was examined (Fig. 3).

The metaheuristic optimization algorithm routine finally means selecting the population values based on the scale and complexity of the optimization task. Whereas the particle swarm algorithm works successfully and effectively with higher population density, the processing complexity grows, since more search spaces are found. The doubt and integrity of the suggested scheme are also

Table 4 Model 2: Results of the PSO-inversion algorithm applied to third horizontal derivative anomalies of the gravity profile (140 km) due to composite anomaly of two-sided dipping fault model (M = 390 mGal, z_{up} = 6 km, $\theta = 40°$, z_{down} = 9 km and $x_0 = 70$ km) and sphere structure (z_{sphere} = 3 km, M_{sphere} = 510 mGal, $x_{o\ sphere}$ = 90 km)

Parameters	Used ranges	Results											
		Noise-free case											
		s = 2km	s = 3 km	s = 4 km	s = 5 km	s = 6 km	s = 7 km	s = 8 km	s = 9 km	s = 10 km	ϕ	Error (%)	RMS error (mGal)
M (mGal)	200–800	390	390	392	388.21	387	393.14	391.05	389	394	390.49 ± 2.29	0.13	0.43
z_{up} (km)	2–9	6	6	5.9	6.1	6	6.2	5.9	5.9	6.2	6.02 ± 0.12	0.37	
θ (degree)	20–120	40	40	40.83	40.08	39.45	38.81	40.79	39.61	40.06	39.96 ± 0.63	0.10	
z_{down} (km)	5–14	9.1	9.1	9.1	8.9	9.1	8.8	9.2	9.1	9	9.04 ± 0.12	0.49	
x_o (km)	60–80	70	70	70.21	69.87	69.74	70.26	70.05	70.31	70.05	70.05 ± 0.18	0.08	
10% random noise case													
M (mGal)	200–800	402	397.11	384	396.62	400	395.06	397.14	394.06	401.04	396.34 ± 5.34	1.62	14.06
z_{up} (km)	2–9	6.6	6.4	6.7	6.4	6.6	6.3	5.7	6.3	6.4	6.38 ± 0.29	6.30	
θ (degree)	20–120	46.05	37.12	44.06	35.74	36.12	44.25	43.54	45.74	43.93	41.84 ± 4.23	4.60	
z_{down} (km)	5–14	9.4	9.6	9.3	8.7	8.8	9.5	9.4	8.7	9.3	9.19 ± 0.36	2.10	
x_o(km)	60–80	71	69.02	69.36	69.65	71	69.49	69.51	70.87	70.92	70.09 ± 0.83	0.13	

Table 5 Model 2: Results of the PSO-inversion algorithm applied to fourth horizontal derivative anomalies of the gravity profile (140 km) due to composite anomaly of two-sided dipping fault model (M = 390 mGal, z_{up} = 6 km, $\theta = 40°$, z_{down} = 9 km and $x_0 = 70$ km) and sphere structure (z_{sphere} = 3 km, M_{sphere} = 510 mGal, $x_{o\ sphere}$ = 90 km)

Parameters	Used ranges	Results											
		Noise-free case											
		s = 2km	s = 3 km	s = 4 km	s = 5 km	s = 6 km	s = 7 km	s = 8 km	s = 9 km	s = 10 km	ϕ	Error (%)	RMS error (mGal)
M (mGal)	200–800	389.83	388.87	391.15	392	390	389.71	391.42	392	388.87	390.43 ± 1.24	0.11	0.79
z_{up} (km)	2–9	6	6.2	5.9	5.8	6.1	5.9	6.2	6.1	6	6.02 ± 0.14	0.37	
Θ (degree)	20–120	40	40.94	40	42.05	40	39.06	41.19	41.99	40.63	40.65 ± 1	1.63	
z_{down} (km)	5–14	9.1	8.9	9.1	8.9	9.1	8.9	9.2	8.9	9	9.01 ± 0.12	0.12	
x_o(km)	60–80	70	69.94	70	69.84	70.14	70.35	70.07	70.14	70.04	70.06 ± 0.14	0.08	
10% random noise case													
M (mGal)	200–800	383.84	397.05	398.36	397	399.18	401.05	398.34	384.34	385	393.8 ± 7.16	0.97	13.68
z_{up} (km)	2–9	6.5	6.4	5.7	6.3	6.4	5.8	5.7	6.4	6.6	6.2 ± 0.36	3.33	
Θ (degree)	20–120	46.24	44.36	43.05	37.26	45.09	38.88	45.71	42.08	37.14	42.2 ± 3.6	5.50	
z_{down} (km)	5–14	9.2	9.3	9.5	9.5	8.6	8.7	9.2	9.4	9.3	9.19 ± 0.33	2.10	
x_o (km)	60–80	71	69.87	70.88	70.71	69.96	70.79	69.47	69.86	70.92	70.38 ± 0.59	0.55	

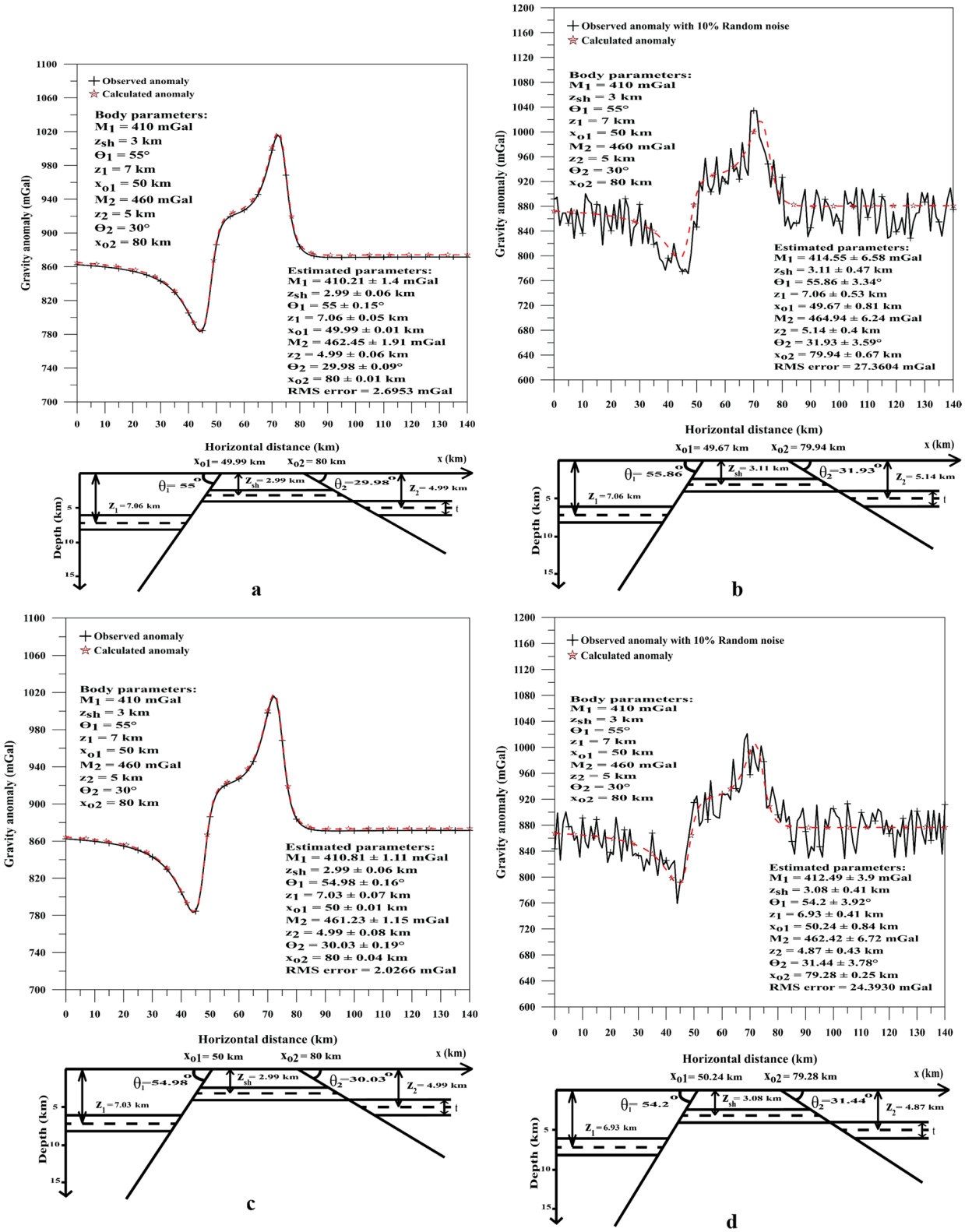

Fig. 6 **a** Gravity anomaly represents Model 3 without noise in case using a third horizontal gradient method. **b** Gravity anomaly represents Model 3 with a 10% noise in case using a third horizontal gradient method. **c** Gravity anomaly represents Model 3 without noise in case using a fourth horizontal gradient method. **d** Gravity anomaly represents Model 3 with a 10% noise in case using a fourth horizontal gradient method. **e** Error percentage in each calculated parameter through Model 1 without and with 10% random noise. **f** Error percentage in each calculated parameter through Model 2 without and with 10% random noise. **g** Error percentage in each calculated parameter through Model 3 without and with 10% random noise

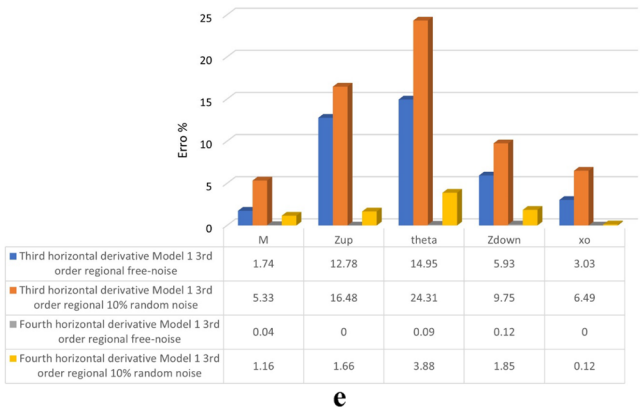

	M	Zup	theta	Zdown	xo
Third horizontal derivative Model 1 3rd order regional free-noise	1.74	12.78	14.95	5.93	3.03
Third horizontal derivative Model 1 3rd order regional 10% random noise	5.33	16.48	24.31	9.75	6.49
Fourth horizontal derivative Model 1 3rd order regional free-noise	0.04	0	0.09	0.12	0
Fourth horizontal derivative Model 1 3rd order regional 10% random noise	1.16	1.66	3.88	1.85	0.12

e

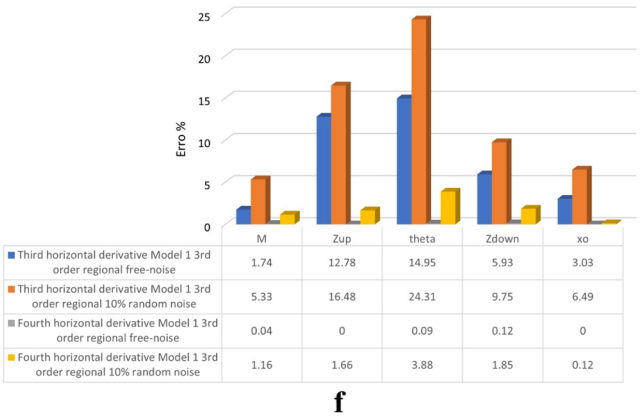

	M	Zup	theta	Zdown	xo
Third horizontal derivative Model 1 3rd order regional free-noise	1.74	12.78	14.95	5.93	3.03
Third horizontal derivative Model 1 3rd order regional 10% random noise	5.33	16.48	24.31	9.75	6.49
Fourth horizontal derivative Model 1 3rd order regional free-noise	0.04	0	0.09	0.12	0
Fourth horizontal derivative Model 1 3rd order regional 10% random noise	1.16	1.66	3.88	1.85	0.12

f

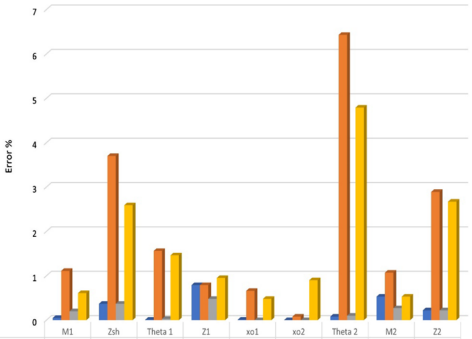

	M1	Zsh	Theta 1	Z1	xo1	xo2	Theta 2	M2	Z2
Third horizontal derivative Model 3 Two neighboring faults free-noise	0.05	0.37	0.01	0.79	0.01	0	0.08	0.53	0.22
Third horizontal derivative Model 3 Two neighboring faults 10% random noise	1.11	3.7	1.56	0.79	0.66	0.08	6.43	1.07	2.89
Fourth horizontal derivative Model 3 Two neighboring faults free-noise	0.2	0.37	0.03	0.48	0	0	0.1	0.27	0.22
Fourth horizontal derivative Model 3 Two neighboring faults 10% random noise	0.61	2.59	1.46	0.95	0.48	0.9	4.79	0.53	2.67

g

Fig. 6 (continued)

explored using the previously mentioned three synthetic models with a 10% random noise and two case studies, as discussed in the following section. To avoid the doubt of the offered method utilizing different values of s windows and each s window through considerable numbers of iterations, then taking the average of the finest parameter values from the whole s windows solutions to get more reliable results.

Field examples

To investigate the rationality and the stability of the offered scheme for the buried fault parameters estimation, two published real data sets of case studies from the United States and Tunisia were used. The particle swarm optimization scheme was implemented to these data to accomplish the optimal fit for the buried fault parameters (M, z_{up}, θ, z_{down}, x_o). The results were then matched with existing geologic information and any additional geophysical outcomes.

Case 1: Seattle fault system, USA

The Puget Lowland is located inside a forearc region of a Cascade subduction region. It is confined by a Cascade Volcanic Arc, the old Mesozoic terrain, and the uplifted and quarried Olympic Mountains accretion complex. The depth of the Puget Lowland approaches 25–30 km and superimposes Siletz terrain, basalts, and invasive rocks, including island-arc formations. The bedrock beneath the tailing basin reached depths between 2.195 and 2.637 km. These bedrocks are basalt embedded in mafic rock interspersed with siltstone, tuff, conglomerate, and sandstone (Symons and Crosson 1997; Rau and Johnson 1999; Brink et al. 2002) (Fig. 7a). Figure 7a indicates the position of the examined area and observed gravity profile. It is crossed over a Seattle fault region, which comprises two steep strata deformed primarily through two or more faults (Johnson et al. 1994). The Seattle fault region has a placement from east–west, depth to subsurface bedrock, and the danger of metropolitan

Table 6 Model 3: Results of the PSO-inversion algorithm applied to third horizontal derivative anomalies of the gravity profile (140 km) due to composite anomaly of two two-sided dipping fault models (M_1 = 410 mGal, z_{sh} = 3 km, z_1 = 7 km, θ_1 = 55°, x_{o1} = 50 km) and (M_2 = 460 mGal, z_{sh} = 3 km, z_1 = 7 km, θ_1 = 55°, x_{o2} = 80 km)

Parameters	Used ranges	Results											
		Noise-free case											
		s = 2 km	s = 3 km	s = 4 km	s = 5 km	s = 6 km	s = 7 km	s = 8 km	s = 9 km	s = 10 km	ϕ	Error (%)	RMS error (mGal)
M_1 (mGal)	200–750	412.13	407.06	410	410	410	410	410.95	411.32	410.39	410.21 ± 1.4	0.05	2.70
z_{sh} (km)	1–6	3	3	3.1	3	3	2.9	3	2.9	3	2.99 ± 0.06	0.37	
θ_1 (degree)	10–100	55.14	55.13	55	55	55	55	55.06	54.63	55	55 ± 0.15	0.01	
z_1 (km)	3–10	7	7	7.1	7.1	7.1	7.1	7	7.1	7	7.06 ± 0.05	0.79	
x_{o1} (km)	30–70	49.99	49.98	50	50	50	50	49.98	50	50	49.99 ± 0.01	0.01	
x_{o2} (km)	60–100	80.01	80.03	79.99	80	80	80	80	80	80	80 ± 0.01	0.00	
θ_2 (degree)	10–100	29.92	29.77	30.06	30	30	30	30	30.01	30.02	29.98 ± 0.09	0.08	
M_2 (mGal)	100–600	463	464.05	462	465.05	461	463	464.21	459.33	460.39	462.45 ± 1.91	0.53	
z_2 (km)	2–8	5	5	5.1	5	4.9	5	5	4.9	5	4.99 ± 0.06	0.22	
10% random noise case													
M_1 (mGal)	200–750	414	415.26	417.88	418	403	419	421	404.05	418.74	414.55 ± 6.58	1.11	27.36
z_{sh} (km)	1–6	2.6	2.6	3.5	3.4	2.7	2.6	3.5	3.7	3.4	3.11 ± 0.47	3.70	
θ_1 (degree)	10–100	58	56.04	59.99	50.74	50	57.95	57.01	57	56	55.86 ± 3.34	1.56	
z_1 (km)	3–10	6.5	7.5	7.6	7.4	6.6	6.5	7.5	7.5	6.4	7.06 ± 0.53	0.79	
x_{o1} (km)	30–70	50	49.03	49	51	49.04	49.31	49.2	51	49.44	49.67 ± 0.81	0.66	
x_{o2} (km)	60–100	79	80.12	80.58	79.49	79.24	81	80.53	79.67	79.79	79.94 ± 0.67	0.08	
θ_2 (degree)	10–100	31.99	34.26	26.32	27.72	28.45	33.07	34	36.55	35	31.93 ± 3.59	6.43	
M_2 (mGal)	100–600	470	465.05	453.27	456.29	464	468	471	469.84	467	464.94 ± 6.24	1.07	
z_2 (km)	2–8	4.7	5.7	5.5	4.9	4.8	4.6	5.4	5.3	5.4	5.14 ± 0.4	2.89	

Table 7 Model 3: Results of the PSO-inversion algorithm applied to fourth horizontal derivative anomalies of the gravity profile (140 km) due to composite anomaly of two two-sided dipping fault models (M_1 = 410 mGal, z_{sh} = 3 km, z_1 = 7 km, $\theta_1 = 55°$, x_{o1} = 50 km) and (M_2 = 460 mGal, z_{sh} = 3 km, z_1 = 7 km, $\theta_1 = 55°$, x_{o2} = 80 km)

Parameters	Used ranges	Results											
		Noise-free case											
		s = 2 km	s = 3 km	s = 4 km	s = 5 km	s = 6 km	s = 7 km	s = 8 km	s = 9 km	s = 10 km	ϕ	Error (%)	RMS error (mGal)
M_1 (mGal)	200–750	410	411	412.99	410	410	412.13	410	410	411.15	410.81 ± 1.11	0.20	2.03
z_{sh} (km)	1–6	3	3.1	3	3	3	2.9	3	3	2.9	2.99 ± 0.06	0.37	
θ_1 (degree)	10–100	55	54.9	55.02	55.23	55.05	54.64	55	55	55	54.98 ± 0.16	0.03	
z_1 (km)	3–10	7.1	7	7	7	7.1	7.1	7	7.1	6.9	7.03 ± 0.07	0.48	
x_{o1} (km)	30–70	50	50.01	49.97	50.01	50	50	50	50	50	50 ± 0.01	0.00	
x_{o2} (km)	60–100	80	80	80.02	79.99	80	79.9	80.06	80	80	80 ± 0.04	0.00	
θ_2 (degree)	10–100	29.99	30	30	29.89	30.52	30	29.87	30	30	30.03 ± 0.19	0.10	
M_2 (mGal)	100–600	462.08	460	461	463.4	461.33	460	462	461.22	460	461.23 ± 1.15	0.27	
z_2 (km)	2–8	5	5.1	5	5.1	5	4.9	4.9	5	4.9	4.99 ± 0.08	0.22	
10% random noise case													
M_1 (mGal)	200–750	413.01	415	414	416.17	407.33	408.1	407	415.79	416	412.49 ± 3.9	0.61	24.39
z_{sh} (km)	1–6	2.8	2.7	2.7	3.4	3.5	3.6	3.5	2.8	2.7	3.08 ± 0.41	2.59	
θ_1 (degree)	10–100	59	57	58.88	57.62	49.11	50.99	52	53	50.19	54.2 ± 3.92	1.46	
z_1 (km)	3–10	7.2	7.3	6.7	7.5	7.4	6.7	6.5	6.6	6.5	6.93 ± 0.41	0.95	
x_{o1} (km)	30–70	51	49.12	49.02	49.41	50.11	50.79	50.8	50.93	51	50.24 ± 0.84	0.48	
x_{o2} (km)	60–100	79.07	79	79.5	79.69	79.52	79.08	79.05	79.28	79.31	79.28 ± 0.25	0.90	
θ_2 (degree)	10–100	27	28	35	32.9	34.66	34.17	27.5	27.71	36	31.44 ± 3.78	4.79	
M_2 (mGal)	100–600	467.03	466	462	467.27	468.52	453.59	452.11	456.25	469.01	462.42 ± 6.72	0.53	
z_2 (km)	2–8	4.5	4.6	4.6	4.5	4.7	4.6	5.4	5.5	5.4	4.87 ± 0.43	2.67	

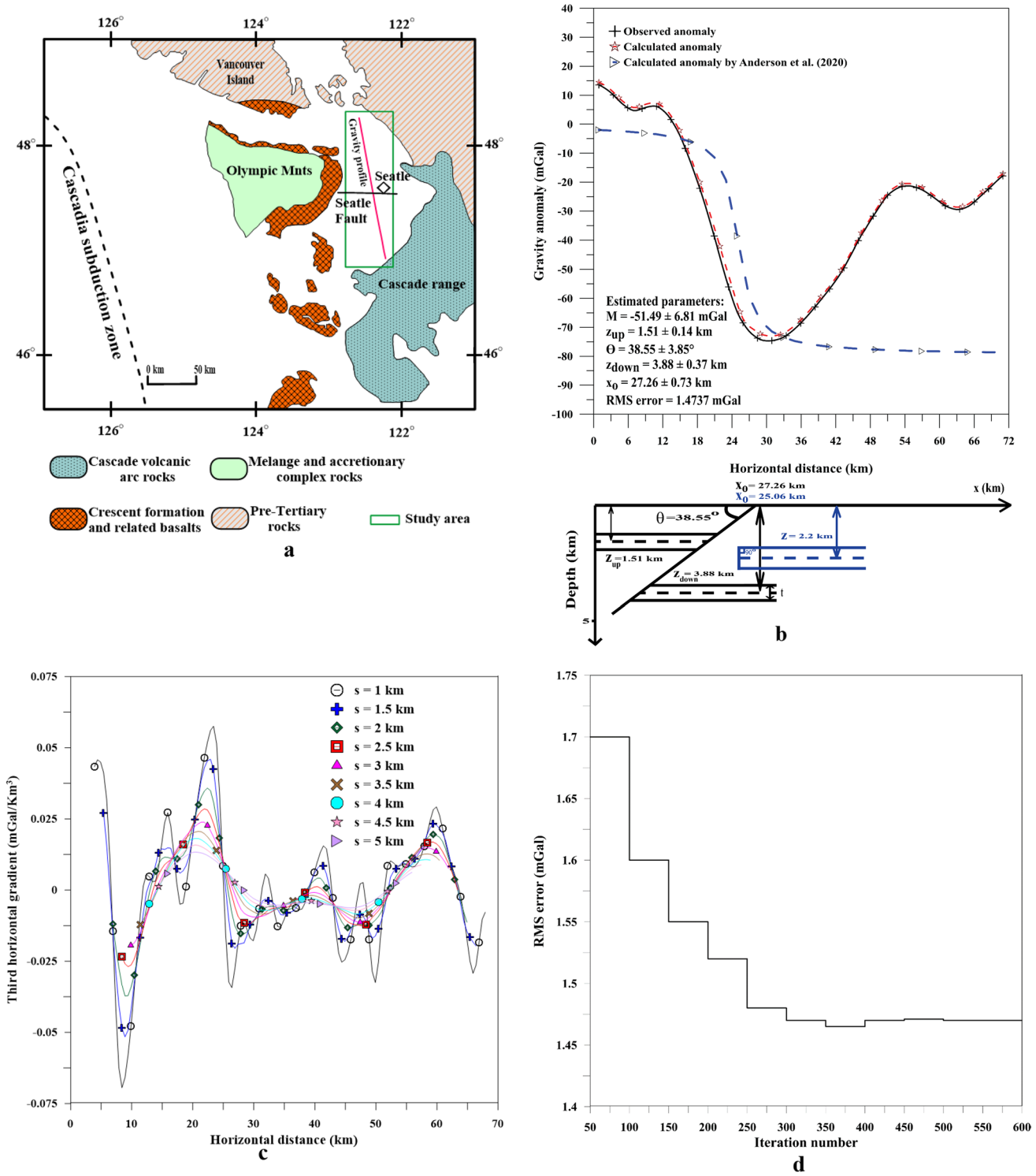

Fig. 7 **a** Case 1: Geological map for the area including the Seattle Fault System, USA (after Brink et al. 2002). **b** Observed and predicted gravity anomalies deduced from using the third horizontal gradient method. **c** Third horizontal derivative anomalies using different s values of **b**. **d** Convergence rate of the PSO scheme after applying the third horizontal gradient method. **e** Observed and predicted gravity anomalies deduced from using the fourth horizontal gradient method. **f** Fourth horizontal derivative anomalies using the s values of **b**. **g** Convergence rate of the PSO scheme after applying the fourth horizontal gradient method

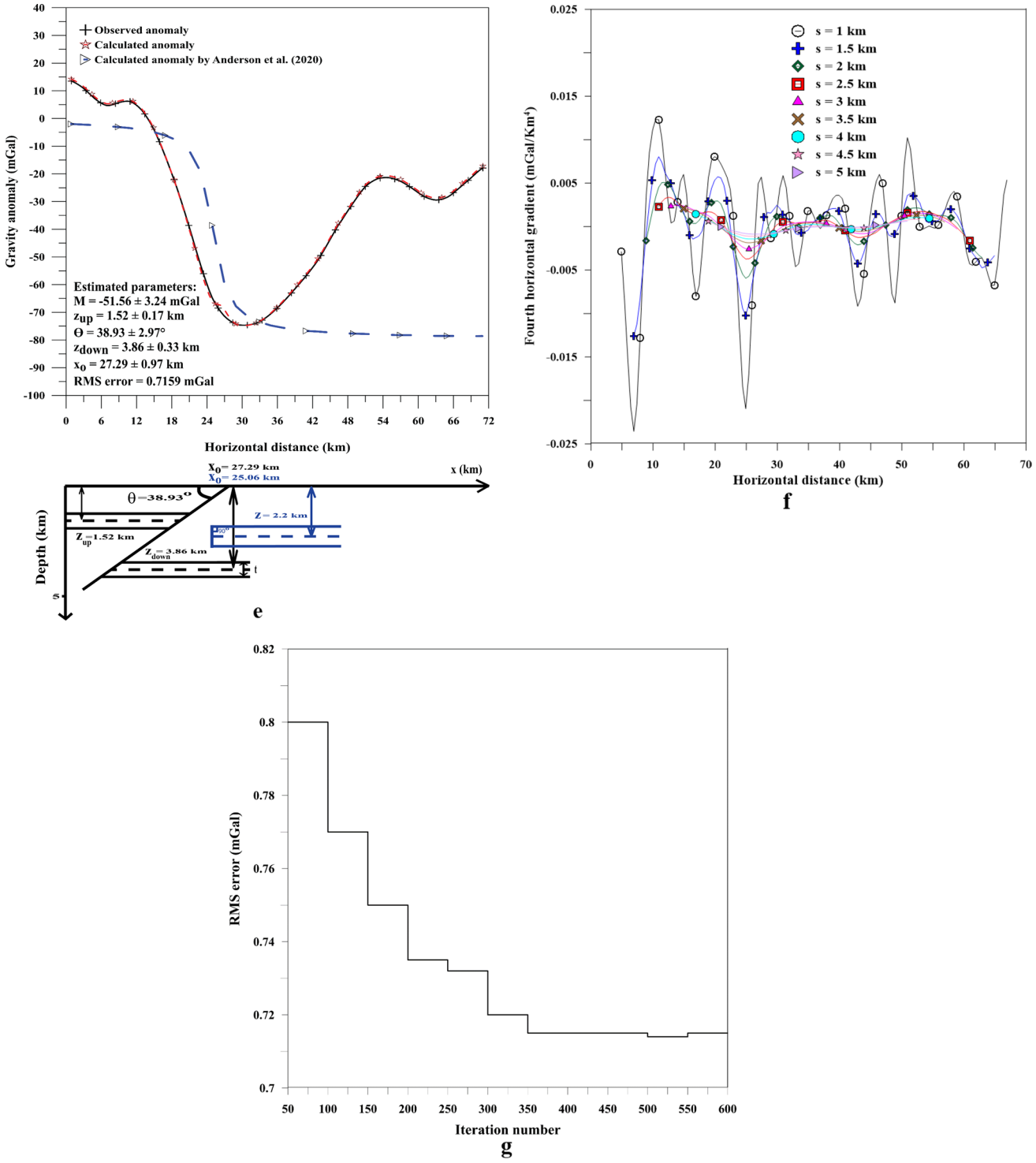

Fig. 7 (continued)

inhabitants' concentration. It is a complex thrust, reversing fault with nearly 7 km width and 70 km length delimiting the northern margin of the Seattle uplift.

Figure 7b shows the observed and estimated anomalies with $M = -51.49 \pm 6.73$ mGal, $z_{up} = 1.51 \pm 0.1$ km, $\theta = 38.55 \pm 3.62°$, $z_{down} = 3.88 \pm 0.37$ km, $x_o = 27.26 \pm 0.87$

Table 8 Results of the PSO-inversion algorithm applied to the third horizontal derivative anomalies of the Seattle fault, USA

Parameters	Used ranges	Results										
		$s=1$ km	$s=1.5$ km	$s=2$ km	$s=2.5$ km	$s=3$ km	$s=3.5$ km	$s=4$ km	$s=4.5$ km	$s=5$ km	ϕ	RMS error (mGal)
M (mGal)	− 420 to 200	− 47.02	− 54.24	− 46.74	− 41.8	− 58.91	− 57.8	− 60.99	− 45.92	− 50	− 51.49 ± 6.73	1.47
z_{up} (km)	0.4–6.5	1.5	1.59	1.61	1.59	1.5	1.45	1.28	1.5	1.6	1.51 ± 0.1	
θ (degree)	10–90	37	34.08	42.33	40	38.07	45.13	39	37.34	34	38.55 ± 3.62	
z_{down} (km)	0.5–8	3.6	3.7	4.3	3.6	3.4	3.8	4.2	4.5	3.8	3.88 ± 0.37	
x_o (km)	25–35	26.9	25.8	27.3	28.4	28.4	26.7	26.5	27.6	27.7	27.26 ± 0.87	

Table 9 Results of the PSO-inversion algorithm applied to the fourth horizontal derivative anomalies of the Seattle fault, USA

Parameters	Used ranges	Results										
		$s=1$ km	$s=1.5$ km	$s=2$ km	$s=2.5$ km	$s=3$ km	$s=3.5$ km	$s=4$ km	$s=4.5$ km	$s=5$ km	ϕ	RMS error (mGal)
M (mGal)	− 420 to 200	− 52.02	− 54.82	− 48.01	− 55	− 48	− 47.45	− 50	− 53.71	− 55.02	− 51.56 ± 3.24	0.72
z_{up} (km)	0.4–6.5	1.74	1.58	1.64	1.29	1.45	1.3	1.6	1.7	1.4	1.52 ± 0.17	
θ (degree)	10–90	37.05	35	42.19	39.2	44.17	36.99	41	36.78	38.01	38.93 ± 2.97	
z_{down} (km)	0.5–8	3.4	3.9	3.8	3.7	3.6	4.2	4.5	3.7	3.9	3.86 ± 0.33	
x_o (km)	25–35	25.9	28.1	28.2	27.1	28.2	28.4	27.1	26.5	26.1	27.29 ± 0.97	

Table 10 Case 1: achieved results of the Seattle fault, USA

Methods	Brink et al. (2002)	Anderson et al. (2020)	Essa et al. (2021b)	Present method
Parameters				
M (mGal)	–	− 72.61 ± 15.74	− 52.28 ± 12.40	− 51.56 ± 3.24
z_{up} (km)	1.5	2.2 ± 0.52	1.46 ± 0.34	1.52 ± 0.17
θ (degree)	40	–	38.75 ± 4.06	38.93 ± 2.97
z_{down} (km)	3.8	–	3.73 ± 0.40	3.86 ± 0.33
x_o (km)	26.5	25.06 ± 0.97	27.03 ± 0.93	27.29 ± 0.97

km) and RMS error equals 1.47 mGal (Table 8). Also, the third horizontal derivative anomalies using different values of s ($s = 1$ km, $s = 1.5$ km, $s = 2$ km, $s = 2.5$ km, $s = 3$ km, $s = 3.5$ km, $s = 4$ km, $s = 4.5$ km, $s = 5$ km) are shown in Fig. 7c. Moreover, the convergence rate of the PSO algorithm demonstrated in Fig. 7d.

In case of utilizing the fourth horizontal gradient, Fig. 7e explains the observed and estimated anomalies with $M = -\ 51.56 \pm 3.24$ mGal, $z_{up} = 1.52 \pm 0.17$ km, $\theta = 38.93 \pm 2.97°$, $z_{down} = 3.86 \pm 0.33$ km, $x_o = 27.29 \pm 0.97$ km) and RMS error is 0.72 mGal (Table 9). In addition, the fourth derivative anomalies are displayed in Fig. 7f for the same s values declared above. Finally, the convergence rate is mentioned in Fig. 7g. A comparison results are demonstrated in Table 10.

Case 2: Bizerte Molassic Basin, Tunisia

Figure 8a, the study area includes a 1:50 km scale geological map of Metline and Porto-Farina, the oldest series of exposures are Triassic evaporates positioned close to the town of El Alia, along the El Alia fault. In the southern district of Metline city, the Upper Cretaceous is signified by "Cenomanian marly limestone, Senonian marls, and Middle Campanian–Lower Maastrichtian marl-limestone alternations and outcrops." Green clays from the El Haria formation are a representative fossil of the Late Maastrichtian–Paleocene. At El Alia, Metline, and Menzel Jemil, huge outcroppings of Globigerina limestone correlate to the lower Eocene deposits. The Middle-Upper Miocene succession was signified through "marls, clays, sandstones, conglomerates, and gypsum layers" (El Ghali and Ben Ayed 2000). In addition, more geologic setting details are found in several published literature (Ben Ayed et al. 1979; Bejaoui et al. 2016; Zaghdoudi et al. 2021).

Figure 8b explains the original and estimated anomalies with $M = -\ 4 \pm 0.79$ mGal, $z_{up} = 0.31 \pm 0.11$ km, $\theta = 78.07 \pm 3.59$o, $z_{down} = 0.94 \pm 0.13$ km, $x_o = 2.01 \pm 0.13$ km, and RMS error equals 1.00 mGal (Table 11). In addition, Fig. 8c shows the third derivative anomalies using different values of s ($s = 0.028$, 0.042, 0.056, 0.070, 0.084, 0.098, 0.112, 0.126, and 0.140 km). Figure 8d shows the convergence rate of the PSO algorithm engaged to third horizontal anomalies.

Finally, Fig. 8 shows the original and estimated anomalies with $M = -\ 3.8 \pm 0.78$ mGal, $z_{up} = 0.32 \pm 0.09$ km, $\theta = 77.97 \pm 4.33°$, $z_{down} = 0.95 \pm 0.2$ km, $x_o = 2.017 \pm 0.15$ km, and RMS error is 0.97 mGal (Table 12). Figure 8f displays the fourth gradient anomalies for similar s values. Moreover, Fig. 8g displays the rate of convergence of the PSO scheme used for fourth horizontal anomalies.

Discussion

Our results of synthetic investigations, which included the weight of the regional field, interference of neighboring structures, and complex fault system, explain that the utilization of a particle swarm optimizer incorporated with the horizontal gradient method (with different orders) can avoid the noise and regional anomaly in the collected gravity data and gives a respected view for deducing the subsurface two-sided fault parameters (the amplitude coefficient, depths of up- and downthrown, dip angle, and fault trace location). Furthermore, the sensitivity error in each parameter (M, z_{up}, θ, z_{down}, x_o) in all synthetic cases is demonstrated in Fig. 6e, f, and g including the effect of noise. Also, attained results for two field cases reflected the accuracy of the existing method.

Gravity anomaly in the Seattle Fault Region (Case 1: USA) for deducing its parameters (Fig. 7b, e) has been investigated. The attained results for this fault structure are matched with available geologic and geophysical information (Table 10). For example, the depths for up- and down-thrown deduced by Brink et al. (2002) equal 1.5 km and 3.5 km, respectively. In addition, depths deduced by Essa et al. (2021b) are 1.46 km and 3.73 km, respectively.

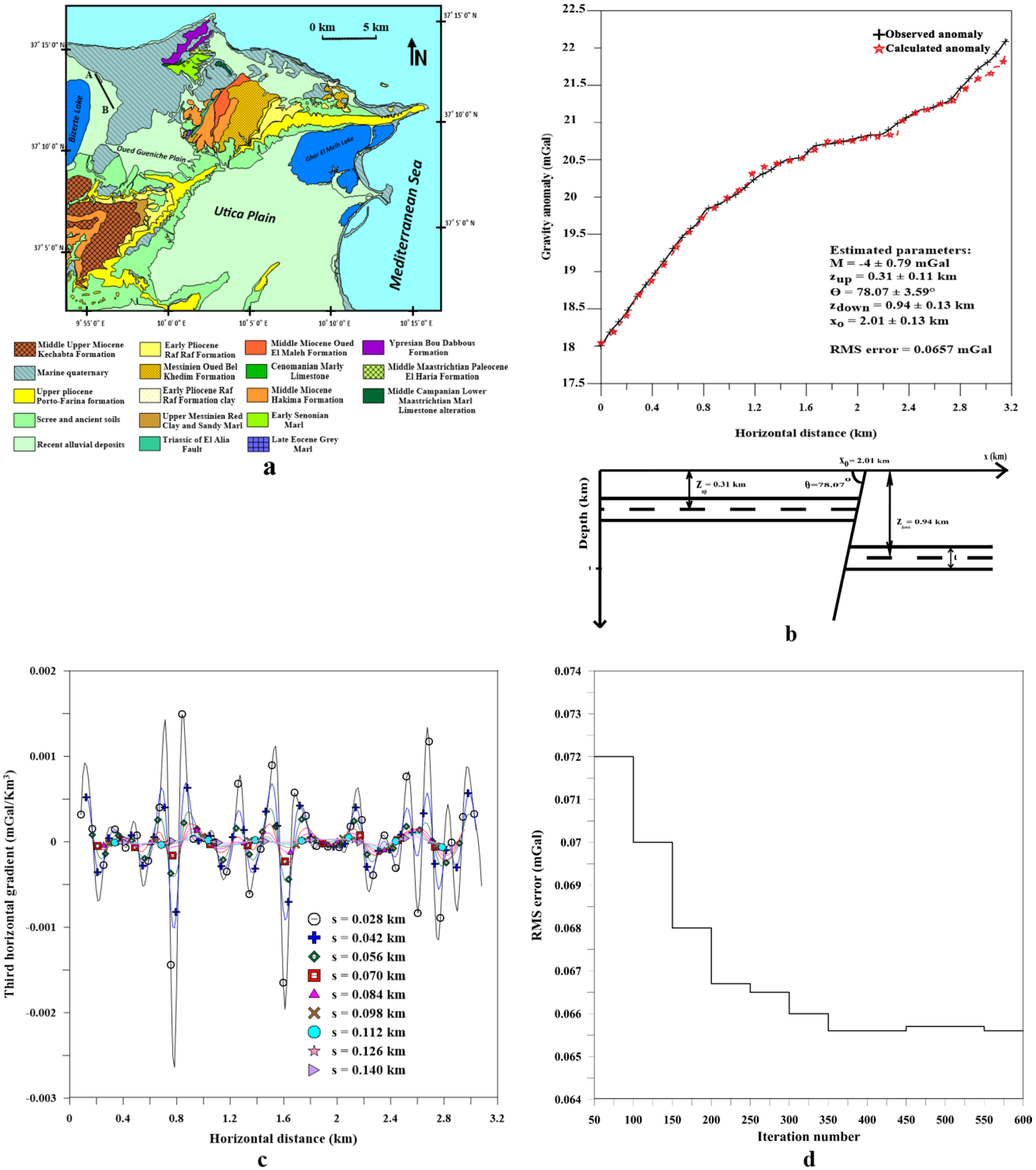

Fig. 8 **a** Case 2: Geological map of the Bizerte Molassic Basin, South of Bizerte City, Northeastern Tunisia (after El Ghali and Ben Ayed 2000; Zaghdoudi et al. 2021). **b** Observed and predicted gravity anomalies deduced from using the third horizontal gradient method. **c** Third horizontal derivative anomalies using different s values of **b**. **d** Convergence rate of the PSO scheme after applying the third horizontal gradient method. **e** Observed and predicted gravity anomalies deduced from using the fourth horizontal gradient method. **f** Fourth horizontal derivative anomalies using the s values of **b**. **g** Convergence rate of the PSO scheme after applying the fourth horizontal gradient method

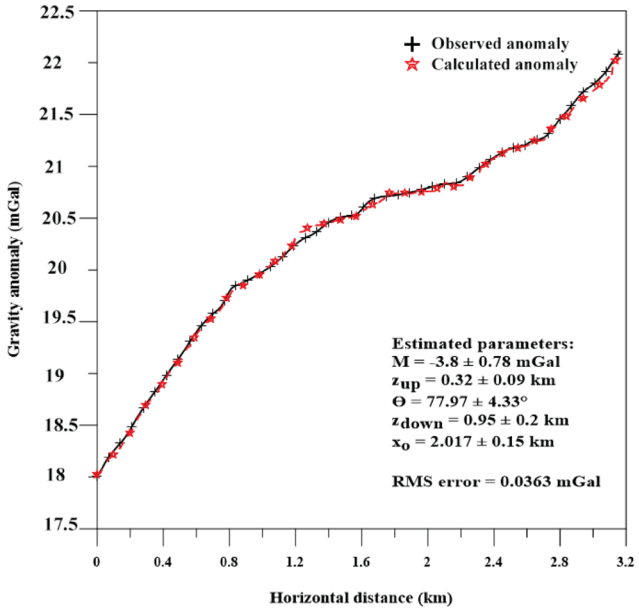

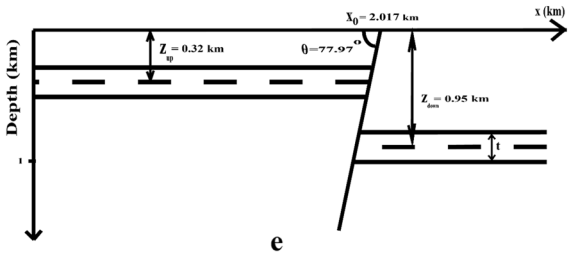

e

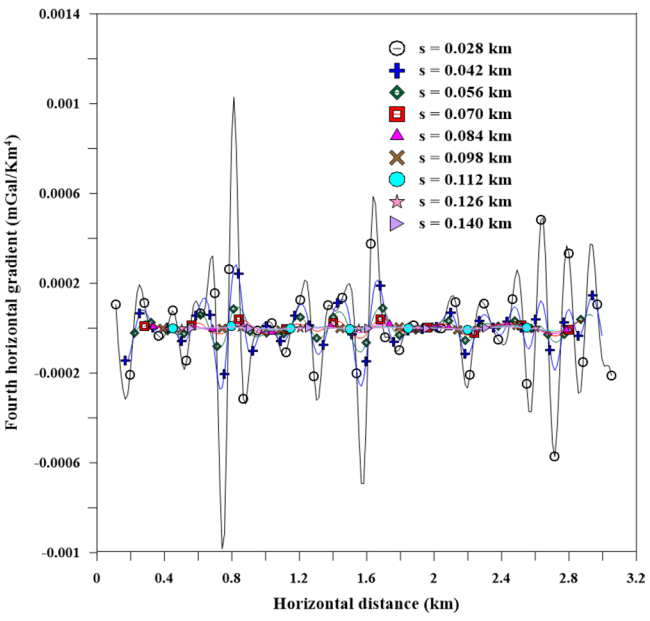

f

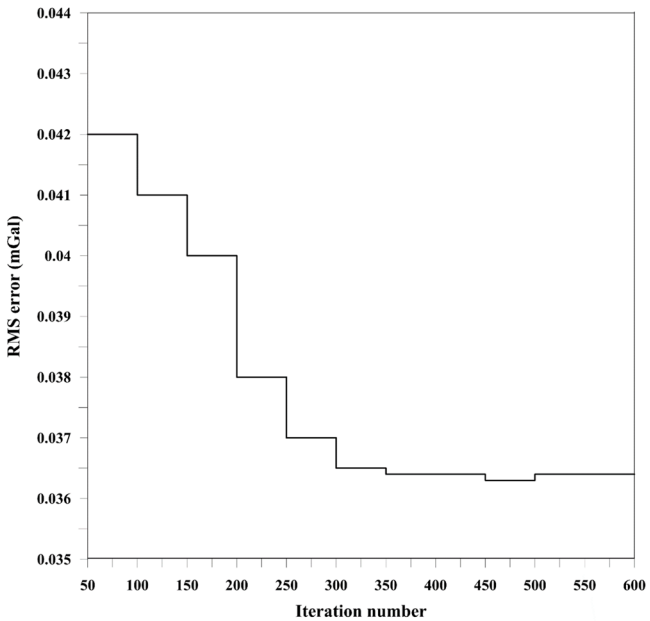

g

Fig. 8 (continued)

Table 11 Results of the PSO-inversion algorithm applied to the third horizontal derivative anomalies of the Bizerte Molassic Basin, Tunisia

Parameters	Used ranges	Results									
		$s = 0.028$ km	$s = 0.042$ km	$s = 0.056$ km	$s = 0.070$ km	$s = 0.084$ km	$s = 0.098$ km	$s = 0.112$ km	$s = 0.126$ km	$s = 0.140$ km	ϕ	RMS error (mGal)
M (mGal)	− 100 to 100	− 3.2	− 5.2	− 4.6	− 4	− 3.1	− 5	− 4	− 3.25	− 3.65	− 4 ± 0.79	1.00
z_{up} (km)	0.1–1.1	0.25	0.2	0.4	0.45	0.3	0.5	0.2	0.27	0.2	0.31 ± 0.11	
θ (degree)	10–90	79.58	78.1	78.9	80	79.98	74.5	70	80.6	81	78.07 ± 3.59	
z_{down} (km)	0.3–1.4	0.95	0.99	1.2	0.86	0.8	1.05	0.78	0.85	0.95	0.94 ± 0.13	
x_o (km)	1–3	1.98	1.8	2.2	2.1	2.01	1.99	1.85	2.04	2.15	2.01 ± 0.13	

Table 12 Results of the PSO-inversion algorithm applied to the fourth horizontal derivative anomalies of the Bizerte Molassic Basin, Tunisia

Parameters	Used ranges	Results									
		$s = 0.028$ km	$s = 0.042$ km	$s = 0.056$ km	$s = 0.070$ km	$s = 0.084$ km	$s = 0.098$ km	$s = 0.112$ km	$s = 0.126$ km	$s = 0.140$ km	ϕ	RMS error (mGal)
M (mGal)	− 100 to 100	− 2.7	− 4	− 5	− 3.6	− 3.6	− 4.4	− 4.2	− 4.1	− 2.6	− 3.8 ± 0.78	0.97
z_{up} (km)	0.1–1.1	0.41	0.25	0.38	0.19	0.3	0.47	0.31	0.3	0.23	0.32 ± 0.09	
θ (degree)	10–90	75.2	76.9	82.5	83.1	76.1	84.2	73.5	77.9	72.3	77.97 ± 4.33	
z_{down} (km)	0.3–1.4	0.98	0.85	0.81	0.78	0.99	1.3	0.98	0.7	1.2	0.95 ± 0.2	
x_o (km)	1–3	2.212	1.785	2.25	2.035	1.871	1.951	1.999	2.021	2.032	2.017 ± 0.15	

Moreover, Anderson et al. (2020) postulated this fault as a one-side vertical fault and deduced the depth as 2.2 km. Therefore, our achieved results were compared with others and found acceptable uncertainties (Table 10). Besides, the gravity anomaly in the Bizerte Molassic Basin (Case 2: Tunisia) for deducing fault parameters (Fig. 8b, e) has been inspected. The accomplished results for this fault structure are matched with available geologic and geophysical information from Zaghdoudi et al. (2021). The patterns of the calculated gravity anomalies in the two cases matched well with the observed anomalies.

Finally, the motivation for exploiting the particle swarm scheme is to capitalize on its benefits in overwhelming the instability and non-uniqueness of the gravity anomalies inversion. In addition, the current algorithm can get a stable and acceptable accuracy for the parameters of fault and can be confirmed by available data from other published literature.

Conclusions

The use of the particle swarm optimizer scheme for identifying and deducing the third and fourth horizontal derivative anomalies is likely to be valuable in the geophysical investigation, because it has numerous advantages, including (1) eliminating the influence of deep-structure (regional anomaly), (2) eradicating the weight of neighboring structures and noise responses, and (3) accurately deducing the two-sided fault source parameters.

The proposed method is simple, automatic, and does not involve any graphical support. The synthetic examples investigated demonstrated that the suggested approach is stable in terms of neighboring effect and noise. It has additionally been successively exploited to two real-world data sets from the United States and Tunisia over faults structures and produced positive results. From the validation of the results, this method is robust and firm. Finally, the implementation of PSO to estimate buried fault parameters using real data sets from the United States and Tunisia provides evidence for the rationality and stability of the proposed scheme. The accuracy of the results obtained using PSO can be used to support informed decision making in any investment projects.

Acknowledgements The authors would like to thank Prof. Olaf Kolditz, Editor, and the two capable expert reviewers for their keen interest, valuable comments on the manuscript, and improvements to this work.

Author contributions ME: Writing–editing, Visualization. ERA-E: revised the manuscript and writing, Figures and Tables preparation. OAG: Writing–editing, Visualization, drawing all Figures and Tables. YG: writing and editing the revised version, Conceptualization, Figures and Tables preparation. KSE: Conceptualization, Methodology, Writing–original draft. All authors read and approved the final manuscript.

Funding Open access funding provided by The Science, Technology & Innovation Funding Authority (STDF) in cooperation with The Egyptian Knowledge Bank (EKB).

Availability of data and materials Data will be available upon request.

Declarations

Conflict of interest No conflict of interests.

References

Abdelrahman EM, Essa KS (2015) Three least-squares minimization approaches to interpret gravity data due to dipping faults. Pure Appl Geophys 172:427–438

Abdelrahman EM, Essa KS, Abo-Ezz ER (2013) A least-squares window curves method to interpret gravity data due to dipping faults. J Geophys Eng 10:025003

Anderson NL, Essa KS, Elhussein M (2020) A comparison study using Particle Swarm Optimization inversion algorithm for gravity anomaly interpretation due to a 2D vertical fault structure. J Appl Geophy 179:104120

Asfahani J, Tlas M (2012) Fair function minimization for direct interpretation of residual gravity anomaly profiles due to spheres and cylinders. Pure Appl Geophys 169:157–165

Bejaoui S, Sciuto F, Karoui-Yaakoub N et al (2016) Evolution des microfaunes pl´eistoc`enes le long de la bordure sud du lac de Bizerte (coupe de Sidi Mansour, Nord-est de la Tunisie): interpretation paleo-environnementale. Ann Paleontol 102:151–159

Ben Ayed N, Bobier C, Paskoff R et al (1979) Sur la tectonique r´ecente de la plage du R'mel a ` l'Est de Bizerte (Tunisie nord-orientale). G´eologie M´editerran´eenne. Tome 6, 423–425 num´ero 4, 1979

Brink US, Molzer PC, Fisher MA et al (2002) Subsurface geometry and evolution of the Seattle Fault zone and the Seattle Basin, Washington. Bull Seismol Soc Am 92:1737–1753

Chakravarthi V, Pramod Kumar M, Ramamma B, Rajeswara Sastry S (2016) Automatic gravity modeling of sedimentary basins by means of polygonal source geometry and exponential density contrast variation: two space domain based algorithms. J Appl Geophys 124:54–61

Chavanidis K, Stampolidis A, Kirmizakis P et al (2022) Gravity survey on the oil-bearing dammam dome (Eastern Saudi Arabia) and its implications. Remote Sens 14:735

Datta D, Shalivahan, Agarwal BNP (2012) Potential field interpretation by total gradient inversion using ant colony optimization. In: SEG Technical Program Expanded Abstracts, pp 1–6

Dilalos S, Alexopoulos JD (2020) The contribution of an urban gravity survey to the determinable perspective of Athens city (Greece) underground structure. SN Appl Sci 2:1797

Eberhart RC, Kennedy J (1995) A new optimizer using particle swarm theory. In: Proceedings of the IEEE The Sixth Symposium on Micro Machine and Human Centre, Nagoya, Japan, pp 39–43

Ekinci YL, Yiğitbaş E (2015) Interpretation of gravity anomalies to delineate some structural features of Biga and Gelibolu peninsulas, and their surroundings (north-west Turkey). Geodin Acta 27:300–319

Ekinci YL, Balakaya C, Gokturkler G, Turan S (2016) Model parameter estimations from residual gravity anomalies due to simple-shaped sources using differential evolution algorithm. J Appl Geophys 129:133–147

Ekinci YL, Balkaya Ç, Göktürkler G, Özyalın S (2021) Gravity data inversion for the basement relief delineation through global optimization: a case study from the Aegean Graben System, western Anatolia, Turkey. Geophys J Int 224:923–944

El Ghali A, Ben Ayed N (2000) Carte geologique n◦3 au 1/50.000 de Metline. Ann Mines et Geol. (Tunisie). Tunisie.

Essa KS (2013) Gravity interpretation of dipping faults using the variance analysis method. J Geophys Eng 10:015003

Essa KS, Diab ZE (2023) Source parameters estimation from gravity data using Bat algorithm with application to geothermal and volcanic activity studies. Int J Environ Sci Technol. https://doi.org/10.1007/s13762-022-04263-z

Essa KS, Diab ZE (2023) Gravity data inversion applying a metaheuristic Bat algorithm for various ore and mineral models. J Geodyn 155:101953

Essa KS, Géraud Y (2020) Parameters estimation from the gravity anomaly caused by the two-dimensional horizontal thin sheet applying the global particle swarm algorithm. J Pet Sci Eng 193:107421

Essa KS, Munschy M (2019) Gravity data interpretation using the particle swarm optimization method with application to mineral exploration. J Earth Syst Sci 128:123

Essa KS, Mehanee SA, Soliman KS, Diab ZA (2020) Gravity profile interpretation using the R-parameter imaging technique with application to ore exploration. Ore Geol Rev 126:103695

Essa KS, Géraud Y, Diraison M (2021a) Fault parameters assessment from the gravity data profiles using the global particle swarm optimization. J Pet Sci Eng 207:109129

Essa KS, Mehanee SA, Elhussein M (2021b) Gravity data interpretation by a two-sided fault-like geologic structure using the global particle swarm technique. Phys Earth Planet Inter 311:106631

Essa KS, Abo-Ezz ER, Géraud Y (2021c) Utilizing the analytical signal method in prospecting gravity anomaly profiles. Environ Earth Sci 80:591. https://doi.org/10.1007/s12665-021-09811-3

Essa KS, Abo-Ezz ER, Géraud Y, Diraison M (2022) A full interpretation applying a metaheuristic particle swarm for gravity data of an active mud diaper, SW Taiwan. J Pet Sci Eng 215:110683

Feng R (2021) Improving uncertainty analysis in well log classification by machine learning with a scaling algorithm. J Pet Sci Eng 196:107995

Gadirov V, Kalkan E, Ozdemir A et al (2022) Use of gravity and magnetic methods in oil and gas exploration: case studies from Azerbaijan. Int J Earth Sci Knowl Appl 4:143–156

Guglielmetti L, Moscariello A (2021) On the use of gravity data in delineating geologic features of interest for geothermal exploration in the Geneva Basin (Switzerland): prospects and limitations. Swiss J Geosci 114:15

Johnson SY, Potter CJ, Armentrout JM (1994) Origin and evolution of the Seattle fault and Seattle basin, Washington. Geology 22:71–74

Kheyrollahi H, Alinia F, Ghods A (2021) Regional magnetic and gravity structures and distribution of mineral deposits in Central Iran: implications for mineral exploration. J Asian Earth Sci 217:104828

Kumar CR, Raj AS, Pathak B et al (2020) High density crustal intrusive bodies beneath Shillong plateau and indo Burmese range of Northeast India revealed by gravity modeling and earthquake data. Phys Earth Planet Inter 307:106555

Mehanee SA (2022) A new scheme for gravity data interpretation by a faulted 2-D horizontal thin block: theory, numerical examples, and real data investigation. IEEE Trans Geosci Remote Sens 60:1–14

Nabighian MN, Ander ME, Grauch VJS et al (2005) Historical development of the gravity method in exploration. Geophysics 70:63ND-89ND

Nibisha VA, Ramamma B, Chakravarthi V (2022) Automatic inversion of magnetic anomalies caused by 2D listric fault sources with arbitrary magnetisation. J Earth Syst Sci 131:265

Rao K, Biswas A (2021) Modeling and uncertainty estimation of gravity anomaly over 2D fault using very fast simulated annealing global optimization. Acta Geophys 69:1735–1751

Rau WW, Johnson SY (1999) Well stratigraphy and correlations western Washington and northwestern Oregon. US Geol Surv Map Invest 1–36:I–2621

Rezaie M (2019) 3D non-smooth inversion of gravity data by zero order minimum entropy stabilizing functional. Phys Earth Planet Inter 294:106275

Rosid MS, Saraswati CB (2020) Implementation 3D inversion of gravity data to identify potential hydrocarbon reservoir zones in West Timor Basin. Sains Malays 49:2065–2072

Roy A, Kumar TS (2021) Gravity inversion of 2D fault having variable density contrast using particle swarm optimization. Geophys Prospect 69:1358–1374

Roy A, Kumar TS, Sharma RK (2022) Structure estimation of 2D listric faults using quadratic Bezier curve for depth varying density distributions. Earth Space Sci 9:e2021EA002061

Saleh S, Saleh A, El Emam AE et al (2022) Detection of archaeological ruins using integrated geophysical surveys at the pyramid of Senusret II, Lahun, Fayoum. Egypt Pure Appl Geophys 179:1981–1993

Singh A, Biswas A (2016) Application of global particle swarm optimization for inversion of residual gravity anomalies over geological bodies with idealized geometries. Nat Resour Res 25:297–314

Symons NP, Crosson RS (1997) Seismic velocity structure of the Puget Sound region from three-dimensional nonlinear tomography. Geophys Res Lett 24:2593–2596

Tlas M, Asfahani J (2018) Interpretation of gravity anomalies due to simple geometric-shaped structures based on quadratic curve regression. Contrib Geophys Geod 48:161–178

Toushmalani R, Saibi H (2015) 3D inversion of gravity data using Cuckoo optimization algorithm. In: SEG Global Meeting Abstracts, pp 217–220

Wang J, Han R, Li W, Cheng R (2022) Principles and application of tunnel gravity full-space positioning and detection method for deep high-density vertical orebodies. Front Earth Sci 10:1–13

Young N, Isaia R, Gottsmann J (2020) Gravimetric constraints on the hydrothermal system of the Campi Flegrei caldera. J Geophys Res Solid Earth 125:e2019JB019231

Zaghdoudi S, Kadri A, Ben Alayet M et al (2021) Genesis and structural arrangement of the collapsed Oued Gueniche plain and the surrounding folds (Neogene molassic basin of Bizerte, northeastern Tunisia): insights from gravity data. J African Earth Sci 174:104053